Hindawi
Geofluids
Volume 2018, Article ID 8715080, 24 pages
https://doi.org/10.1155/2018/8715080

*Research Article*

# Hydrogeochemical Characteristics and Geothermometry Applications of Thermal Waters in Coastal Xinzhou and Shenzao Geothermal Fields, Guangdong, China

**Xiao Wang**[1], **Guoping Lu**[1,2] **and Bill X. Hu**[2]

[1]*School of Environmental Studies, China University of Geosciences, Wuhan, Hubei 430074, China*
[2]*Institute of Groundwater and Earth Sciences, Jinan University, 601 Huangpu Ave., Guangzhou, Guangdong 510632, China*

Correspondence should be addressed to Guoping Lu; guopinglu@yahoo.com

Received 11 September 2017; Revised 17 November 2017; Accepted 4 January 2018; Published 31 January 2018

Academic Editor: Aref Lashin



Two separate groups of geothermal waters have been identified in the coastal region of Guangdong, China. One is Xinzhou thermal water of regional groundwater flow system in a granite batholith and the other is thermal water derived from shallow coastal aquifers in Shenzao geothermal field, characterized by high salinity. The hydrochemical characteristics of the thermal waters were examined and characterized as Na-Cl and Ca-Na-Cl types, which are very similar to that of seawater. The hydrochemical evolution is revealed by analyzing the correlations of components versus Cl and their relative changes for different water samples, reflecting different extents of water-rock interactions and clear mixing trends with seawaters. Nevertheless, isotopic data indicate that thermal waters are all of the meteoric origins. Isotopic data also allowed determination of different recharge elevations and presentation of different mixing proportions of seawater with thermal waters. The reservoir temperatures were estimated by chemical geothermometries and validated by fluid-mineral equilibrium calculations. The most reliable estimates of reservoir temperature lie in the range of 148–162°C for Xinzhou and the range of 135–144°C for Shenzao thermal waters, based on the retrograde and prograde solubilities of anhydrite and chalcedony. Finally, a schematic cross-sectional fault-hydrology conceptual model was proposed.

## 1. Introduction

Geothermal systems located along coastal regions have been widely documented around the world, in which thermal waters differ considerably from one system to another in the hydrochemical characteristics and their relationship to salinity. The coastal thermal waters at northern Republic of Djibouti [1], Greece [2, 3], Turkey [4–6], and West Coast of India [7] are significantly affected by seawater, resulting in high salinity. However, despite being coastal geothermal systems, the coastal thermal waters at North Chile [8] and Sri Lanka Island [9], for instance, are much more diluted by the respective local meteoric fresh water, and those with high salinity appeared to be related to water-rock interactions [10] and mixing with brine [5] instead of seawater.

The recharge resources and mixing trends of thermal waters are reflected in the large diversity of ionic compositions and influences of water-rock interactions. Therefore, an overall assessment of the formation and geochemical processes of thermal waters is necessary to quantify the saline contribution from seawater and aid the development and protection of these geothermal resources.

As an important part of the coastal geothermal belt in southern China, Guangdong province located in the hinterland of the Cathaysia Block along the SE margin of the South China Block is characterized by numerous high-temperature hydrothermal systems [11–13]. This area is abundant in the geothermal resource, second only to the geothermal regions in Yunnan and Tibet of southwest China [14, 15]. The presence of more than 300 hot springs with a temperature range of 50–100°C indicates a significant geothermal potential in Guangdong. Multistage magma and repeated activity of deep faults play a controlling role in the formation of geothermal resources [11].

Since the 1980s, geothermal studies undertaken in this area were mainly tasked with the general geological properties, particularly with the focus on tectonic settings of the geothermal activity [18–20]. Based on chemical and stable isotope analysis, the geochemical study from Yuan et al. [11] concluded that the thermal water is the meteoric origin and the possible water-rock interaction processes that occur under different scenarios. Chen et al. [21] suggest a significant amount of reservoir recharge by seawater intrusion, based exclusively on measured Na/Cl ratios. Guo et al. [22] compared different geothermometers to assess the temperature of reservoirs. However, little attempt has been made thus far to study the formation and evolution of thermal waters and to develop the hydrogeochemical properties and a model of the typical hydrothermal system, especially for those in the coastal area.

The main purpose of this study is to reveal the hydrogeochemical evolution of thermal waters in the coastal region of southwest Guangdong province. Geological, hydrochemical, and isotopic characterization of thermal waters was examined to constrain the physical and chemical processes of the deep regional groundwater flow system. Subsurface thermal reservoir temperature estimations were checked for different methods and verified to provide references in similar cases. A regional-scale groundwater flow system proposed in this paper can help explain the genesis of the geothermal system, which is useful for formation mechanism, better management, and utilization of geothermal resources.

## 2. Geological and Hydrogeological Settings

*2.1. Xinzhou Geothermal Field.* The Xinzhou geothermal field, with the highest temperatures measured at spring outlets in Guangdong, is located to the northwest of Xinzhou township, Yangdong county of Guangdong province (Figure 1). The study area lies between longitudes 112°07′ to 112°40′ E and latitudes 21°70′ to 22°00′ N, covering an area of approximately 900 km$^2$. Xinzhou basin is topographically high in the west and east and gradually decreases in elevation from north to south: from the mountainous area and upland to alluvial plain terraces extending into the South China Sea. The region has a southern subtropical monsoon climate, with an annual mean air temperature of 22.5°C, mean rainfall of 2383.2 mm, and mean potential evaporation of 1506.3 mm.

Tectonically, the study area belongs to the Caledonian fold belt of the South China Block, with the intensive repeated activity of deep faults and multistage magmatism (Figure 1). Regional setting exposes multiple granitic magmatisms, including Caledonian, Indosinian, Yanshanian, and Himalayan. Mesozoic Indosinian granitoids are the main intrusive rocks, supplying a most suitable basement for the geothermal systems (Figure 2). The basement consists of Jurassic and Cretaceous biotite granites and granite porphyry which are covered by Miocene volcanic and Holocene and Late Pleistocene fluviodeltaic sediments (Figure 2) [28]. These granitoids have been interpreted as predominantly from the K-rich calc-alkaline series and as I-type rocks caused either by the low-angle rapid subduction of the Paleo-Pacific Plate or by intraplate magmatism [12]. The Xinzhou pluton rocks comprise a diverse variety of rock types, ranging from hornblende granite, adamellite, and biotite granite to tonalite. Peraluminous granitoids formed by crustal melting are also common. They are composed mainly of K-feldspar, plagioclase, quartz, biotite, and amphibole and contain minor amounts of zircon, apatite, titanite, and fluorite. Biotite has been actively replaced by secondary chlorite as an alteration product [12, 20]. As for basement rocks, previous studies [18] confirm that these granites commonly contain relatively higher radioactive U, Th, and K contents, giving a weighted mean radiogenic heat production rate of 6.77 $\mu$W/m$^3$, which provides superior conditions for geothermal resources. In addition, as pointed out by Zhou and Li [19], the granites are closely associated with several deep faults. Granite rocks close to the fault zones are highly fractured and extremely hydrothermally altered in the study area. These tectonic features have led to the formation of several E-W faults and NE-striking deep faults extending approximately up to 400 km, which can act as preferential channels for convective circulation of hydrothermal fluids and exert primary control on geothermal activities.

Numerous surface hydrothermal manifestations including hot springs, steaming ground, and intensified hydrothermal alterations occur in the Xinzhou geothermal field. Most of the hydrothermal active areas of the field are located in the conjunctions between the faults or on the edge of the granitic rock. As reported by Bureau of Geology and Mineral Resources of Guangdong Province [16], there had been more than 85 spots of hot springs with a total discharge rate up to 17.94 L/s, but most of these hot springs have gone dry due to geothermal well drilling. A number of deep wells and thermal wells were drilled by the Institute of Hydrogeology of Guangdong Province, with hot waters and steam flowing up under their own pressure. Volcanic host rocks have hydrothermally been altered and can be divided into four parts vertically: kaolinization, chloritization, epidotization, and silicification.

*2.2. Shenzao Geothermal Field.* The Shenzao geothermal field is located in the tidal zone along the coastline to the southeast of Xinzhou basin. Consequently, the thermal water is characterized by high salinity due to seawater intrusion into coastal aquifers. It is worth noting that the geographical and climatic features of the Shenzao field are very similar to those of the Xinzhou field, with a typically subtropical oceanic climate and various NNE- to NE-trending folds and fractures. The strata outcropping in the Shenzao area include Early and Late Yanshanian biotite granite and biotite granite porphyry and Cambrian shale and silicalites (Figure 1). A variety of Holocene and Late Pleistocene sediments consist of alluvial and lacustrine sands, sandy gravels, and silty sands to silty clay, deposited in supratidal, transitional-marine, and lagoonal settings. A regional approximately NW-striking deep fault passes nearby Zhenghai Bay and extends to the South China Sea, allowing the formation of discharge conduits for water ascending from deep depths.

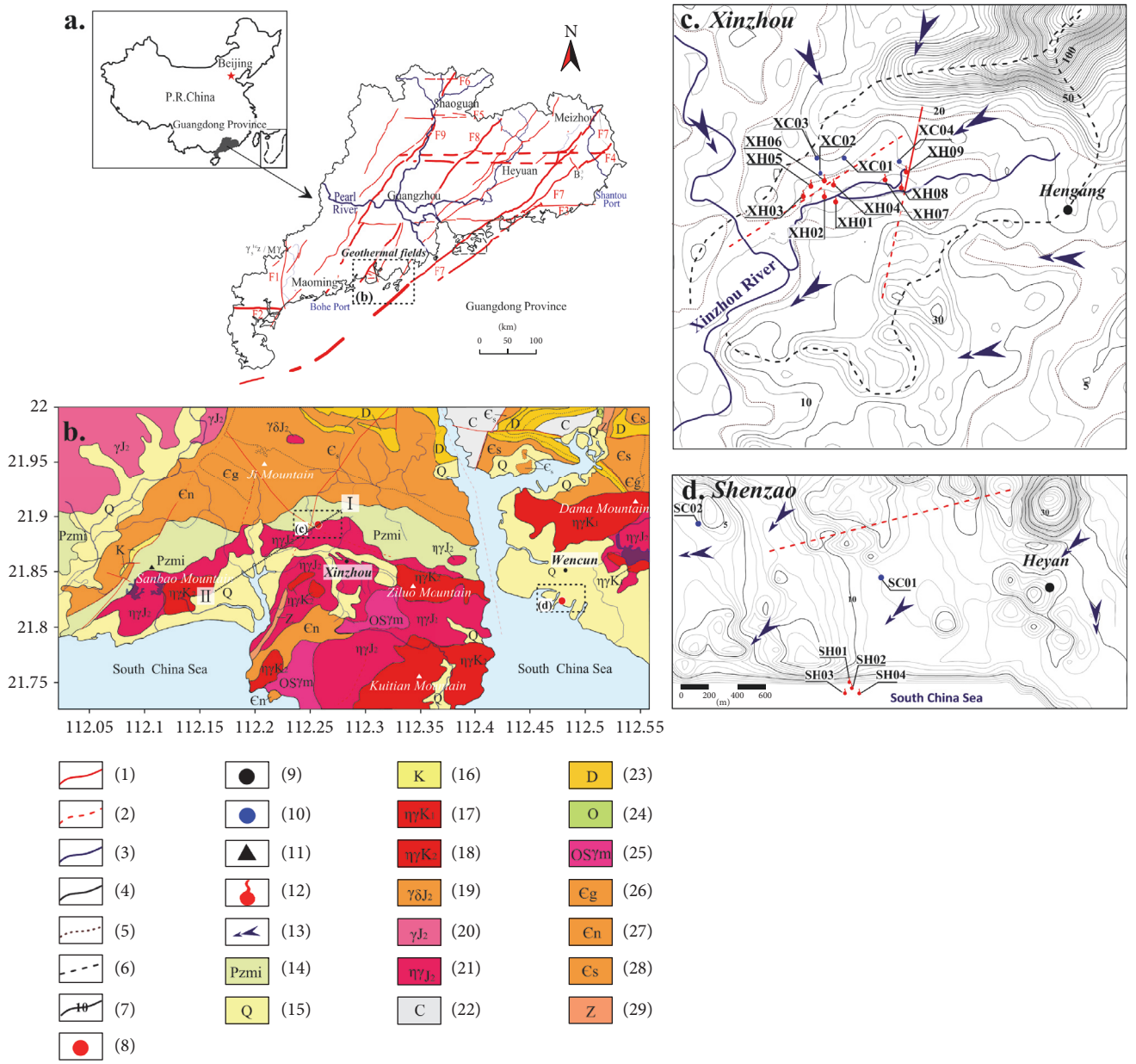


FIGURE 1: Regional bedrock geological map and water sampling locations of the study area. (1) Fault; (2) probable fault; (3) river; (4) stratigraphic boundary; (5) stratigraphic boundary (same period); (6) basin boundary; (7) elevation contour line; (8) geothermal fields; (9) town; (10) cold groundwater sampling site; (11) mountain; (12) thermal groundwater sampling site; (13) nonthermal groundwater flow direction; (14) Paleozoic migmatite; (15) alluvium, proluvium, and marine deposits (Quaternary); (16) sandstone and conglomerate (Cretaceous); (17) biotite monzonitic granite (Early Cretaceous); (18) biotite monzonitic granite (late Cretaceous); (19) granodiorite (Middle Jurassic); (20) medium-grained granite (Middle Jurassic); (21) biotite monzonitic granite (Middle Jurassic); (22) sandstone, siltite, and shale (Carboniferous); (23) shale, conglomerate, and siltite intercalated with limestone (Devonian); (24) siliceous shale and mudstone (Ordovician); (25) migmatitic granite (Ordovician-Silurian); (26) sandstone and shale intercalated with limestone lenses (Cambrian); (27) sandstone, carbonaceous shale, and schist (Cambrian); (28) sandstone and siltite intercalated with carbonaceous shale (Cambrian); and (29) quartz schist and slate (Sinian). Geological data from the Guangdong Province Geological Bureau (1988) [16].

There are four geothermal wells drilled in the coastal aquifers with outflow temperatures higher than 80°C. In addition to the characteristics of geothermal factors including geothermal gradients, reservoir properties, and hydrothermal alteration types (which are similar to those of the Xinzhou field), the thermal water of Shenzao is strongly influenced by a tidally forced moving interface between saltwater and fresh water. Because of the sinusoidal groundwater-level fluctuation pattern, in response to the periodic rise and fall of the tidewater stage in the ocean, geothermal fluidic flow in this area changes cyclically under solid tidal waves [29].

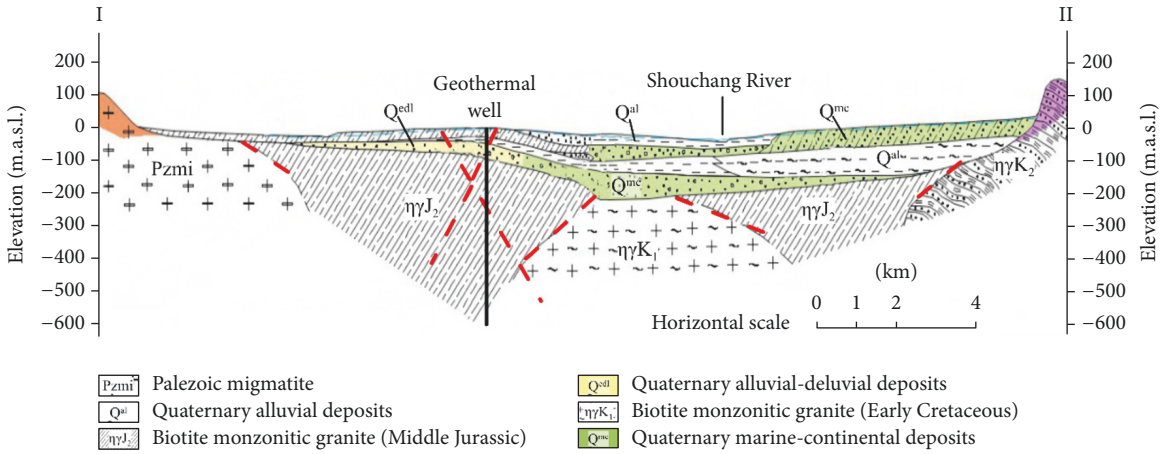


FIGURE 2: Simplified geological cross section along the I-II line (Figure 1(b)) of the study area.

## 3. Materials and Methods

*3.1. Sampling and Analysis.* Hydrogeochemical data and stable isotopic tracers were used to investigate the origin and evolution of thermal water in this area. Water samples of hot springs and boreholes were collected from sites in the northwest and southeast parts of the semicircular Xinzhou basin. Xinzhou's hot springs are naturally exposed along the stream bed, which occur in association with a fault zone. Geothermal wells in the deeper part of the spring are artesian wells, with hot waters and steam flowing up under their own pressure. The average measured wellhead temperatures range between 71 and 98°C and the discharges of these wells are between 86 and 1959 $m^3$/d.

A total of thirteen thermal water samples and six nonthermal water samples were collected in August 2014. Nine of the thirteen thermal water samples were collected from the Xinzhou geothermal field (one tapped spring and eight boreholes), and the other four were collected from the Shenzao geothermal field (all from boreholes). Coastal thermal waters were collected at very low tide when these waters upwelled without any mixing with surface seawater. For comparison purpose, six nonthermal samples of different types were also collected from nearby the geothermal fields, including four shallow groundwater samples, one rainwater sample, and one seawater sample from the South China Sea. The sampling locations and information of geothermal wells are shown and listed in Figures 1(c) and 1(d) and Table 1, respectively.

All the water samples were filtered on-site through 0.45 $\mu$m membrane filters before collection in new 50 ml polyethylene bottles that had been prewashed twice in deionized water. Samples for cation and trace element were acidified with ultrapure $HNO_3$ to a pH less than 2, and the others were kept unacidified for anion analysis. All samples were placed in a portable cooler (4°C) and transported to the laboratory at China University of Geosciences (Wuhan) and stored at 3°C until further analyses.

Unstable hydrochemical parameters including temperature, pH, oxidation-reduction potential (Eh), dissolved oxygen (DO), and electrical conductivity (EC) were measured in the field using a WTW Multi 3400i multiparameter portable field meter. Total alkalinity was also measured in the field by titration with 0.05 mol/L HCl using the Gran titration method [30].

Anion species (Cl, $SO_4$, and $NO_3$) were determined using ion chromatography (Dionex ICS-1100), while cations (K, Na, Ca, and Mg) were determined by inductively coupled plasma-optical emission spectrometry (ICP-OES) (Thermo Fisher ICAP-6300). Inductively coupled plasma mass spectrometry (ICP-MS) (AGILENT 7500a) was applied to the determination of minor elements (e.g., F, Sr, and Li) in the Environmental Chemistry Laboratory, China University of Geosciences (Wuhan), within two weeks after sampling. The water samples are generally of high analytical accuracy, and the charge imbalances of most Xinzhou samples are less than or around 5%, while the other thermal water samples from Shenzao have charge imbalances more than 5% with the highest being up to 8.46%. The charge imbalances in some samples may result from the lack of accurate analysis of dissolved inorganic carbon (DIC) because $CO_2$(g) was lost during sample collection, storage, and analysis [31].

The stable isotope compositions ($^2$H and $^{18}$O) in water samples were measured by the Isotopic Water Analyzer (IWA-35EP) in the State Key Laboratory of Biogeology and Environmental Geology, China University of Geosciences (Wuhan). The $\delta^2$H and $\delta^{18}$O values were reported relative to VSMOW (Vienna Standard Mean Ocean Water) using conventional $\delta$(‰) notation. The precisions for $\delta^2$H and $\delta^{18}$O were ±0.6 and ±0.2‰, respectively.

*3.2. Estimation of Reservoir Temperature.* Quantitative solute geothermometers with empirical equations have been proposed and applied to estimate the probable minimum subsurface temperature based on chemical constituents in thermal water during the past three decades [25, 26, 32]. Some cationic geothermometers can be used to reflect the hot phase equilibrium temperature stored in the geothermal reservoir based on specific chemical reactions, related to temperature-dependent cation exchange and silica solubility between

Table 1: Information of geothermal wells in Xinzhou and Shenzao geothermal fields.

| Label | Name | Date | Wellhead temperature (°C) | Well depth (m) | Water level (m) | Discharge rate ($m^3$/d) | Drilling date |
|---|---|---|---|---|---|---|---|
| *In Xinzhou geothermal field* | | | | | | | |
| XH01 | New hole | 9/8/2014 | 95 | 1000 | 13.7 | 1959 | Dec., 2012 |
| XH02 | Dun | 9/8/2014 | 95 | 298 | 12.3 | 1600 | Dec., 2011 |
| XH03 | Ta | 13/8/2014 | 98 | 350 | 8.7 | 790 | Dec., 2008 |
| XH04 | Jia | 5/8/2014 | 98 | 209 | 7.2 | 447 | Oct., 2008 |
| XH05 | Dongwei | 14/8/2014 | 71 | 280 | 4 | 219 | Dec., 2003 |
| XH07 | Old hole | 14/8/2014 | 81 | 299 | 1.3 | 110 | Dec., 2003 |
| *In Shenzao geothermal field* | | | | | | | |
| SH01 | Shenan | 26/8/2014 | 81 | 100 | 2.2 | 235 | Sep., 2012 |
| SH02 | Shenzhong | 26/8/2014 | 82 | 104 | 1.2 | 86 | Sep., 2012 |
| SH03 | Shenli | 27/8/2014 | 80 | 112 | 1.5 | 147 | Oct., 2012 |
| SH04 | Shenhai | 27/8/2014 | 81 | 139 | 3.5 | 319 | Oct., 2012 |

Table 2: Physicochemical properties of water samples from Xinzhou and Shenzao (elevation in m, temperature in °C, EC in mS/cm, DO in mg/L, flow in L/s, TDS in mg/L, and ORP in mV).

| Label | Name | Date | Type | Ele. | *T* | Flow | pH | TDS | EC | DO | ORP | Hydrochemical type |
|---|---|---|---|---|---|---|---|---|---|---|---|---|
| *In Xinzhou geothermal field* | | | | | | | | | | | | |
| XH01 | New hole | 9/8/2014 | TD | 12 | 95.1 | 0.8 | 8.01 | 3029.39 | 4.78 | 2.83 | −182 | Na-Cl |
| XH02 | Dun | 9/8/2014 | TD | 17 | 94.6 | 0.6 | 7.95 | 3124.17 | 4.34 | 3.46 | −156 | Na-Cl |
| XH03 | Ta | 13/8/2014 | TD | 28 | 97.5 | 0.6 | 8.22 | 3072.23 | 4.97 | 4.69 | −167 | Na-Cl |
| XH04 | Jia | 5/8/2014 | TD | 15 | 98.3 | 0.4 | 8.28 | 3262.68 | 4.96 | 3.94 | −115 | Na-Cl |
| XH05 | Dongwei | 14/8/2014 | TD | 10 | 70.8 | 0.6 | 7.92 | 2712.29 | 4.12 | 4.52 | −172 | Na-Cl |
| XH06 | Dongmao | 14/8/2014 | HS | 33 | 59.5 | N/A | 8.23 | 2355.95 | 3.61 | 5.83 | −187 | Na-Cl |
| XH07 | Old hole | 14/8/2014 | TD | 19 | 81.1 | 0.1 | 8.15 | 1088.50 | 2.05 | 4.08 | −178 | Na-Cl |
| XH08 | Xiting | 17/8/2014 | TD | 24 | 87.0 | 0.8 | 8.17 | 2865.23 | 4.32 | 3.81 | −166 | Na-Cl |
| XH09 | Dongtang | 13/8/2014 | TD | 21 | 79.2 | 0.5 | 8.24 | 2478.91 | 4.61 | 4.55 | −163 | Na-Cl |
| XC01 | Shanbian | 5/8/2014 | AW | 33 | 26.3 | N/A | 7.51 | 230.39 | 0.28 | 4.72 | −256 | Ca-$HCO_3$ |
| XC02 | Cunjin | 5/8/2014 | AW | 38 | 30.1 | N/A | 6.53 | 130.18 | 0.34 | 4.90 | −230 | Ca-Na-$HCO_3$-Cl |
| XC03 | Huangquan | 5/8/2014 | AW | 19 | 42.4 | N/A | 6.89 | 369.88 | 0.34 | — | −231 | Ca-Na-$SO_4$-Cl |
| XC04 | Weijin | 17/8/2014 | AW | 40 | 27.0 | N/A | 6.22 | 327.06 | 0.32 | 5.91 | −233 | Ca-Na-$SO_4$-Cl |
| *In Shenzao geothermal field* | | | | | | | | | | | | |
| SH01 | Shenan | 24/8/2014 | TD | 13 | 81.4 | 3.0 | 7.35 | 9008.30 | 14.20 | 4.10 | −110 | Ca-Na-Cl |
| SH02 | Shenzhong | 24/8/2014 | TD | 16 | 82.3 | 1.1 | 7.71 | 9027.51 | 14.72 | 5.23 | −132 | Ca-Na-Cl |
| SH03 | Shenli | 25/8/2014 | TD | 8 | 79.8 | 1.4 | 7.60 | 9470.66 | 14.80 | 4.90 | −102 | Ca-Na-Cl |
| SH04 | Shenhai | 27/8/2014 | TD | 5 | 81.2 | 3.0 | 7.74 | 8803.77 | 14.12 | 5.19 | −93 | Ca-Na-Cl |
| SC01 | Haiyan | 27/8/2014 | RF | — | 27.0 | N/A | 7.35 | 21.03 | 0.05 | — | — | Ca-Na-$HCO_3$ |
| SC02 | Zhenhai | 19/8/2014 | SW | 0 | 26.0 | N/A | 7.84 | 23951.66 | 25.97 | 2.40 | −109 | Na-Cl |

TD, thermal drill; HS, hot spring; AW, agricultural well; RF, rainfall; SW, seawater; N/A, not applicable.

mineral and solute [33]. In this paper, several widely used solute geothermometers (Na-K, K-Mg, quartz, and chalcedony), together with fluid-mineral equilibria calculations, were used to give a preliminary prediction of the reservoir temperatures. The equilibrium state between thermal water and specific minerals was studied using Na-K-Mg triangular diagram, activity diagram, and saturation index (SI) diagrams.

## 4. Results and Discussion

### 4.1. Origin and Evolution of the Geothermal Waters

*4.1.1. Physiochemical Parameters.* Table 2 shows that the average *T*, pH, conductivity (EC), and total dissolved solids (TDS) values are much lower in cold groundwater (31.44°C, 6.79, 0.32 mS/cm, and 156.75 mg/L, resp.), whereas DO values

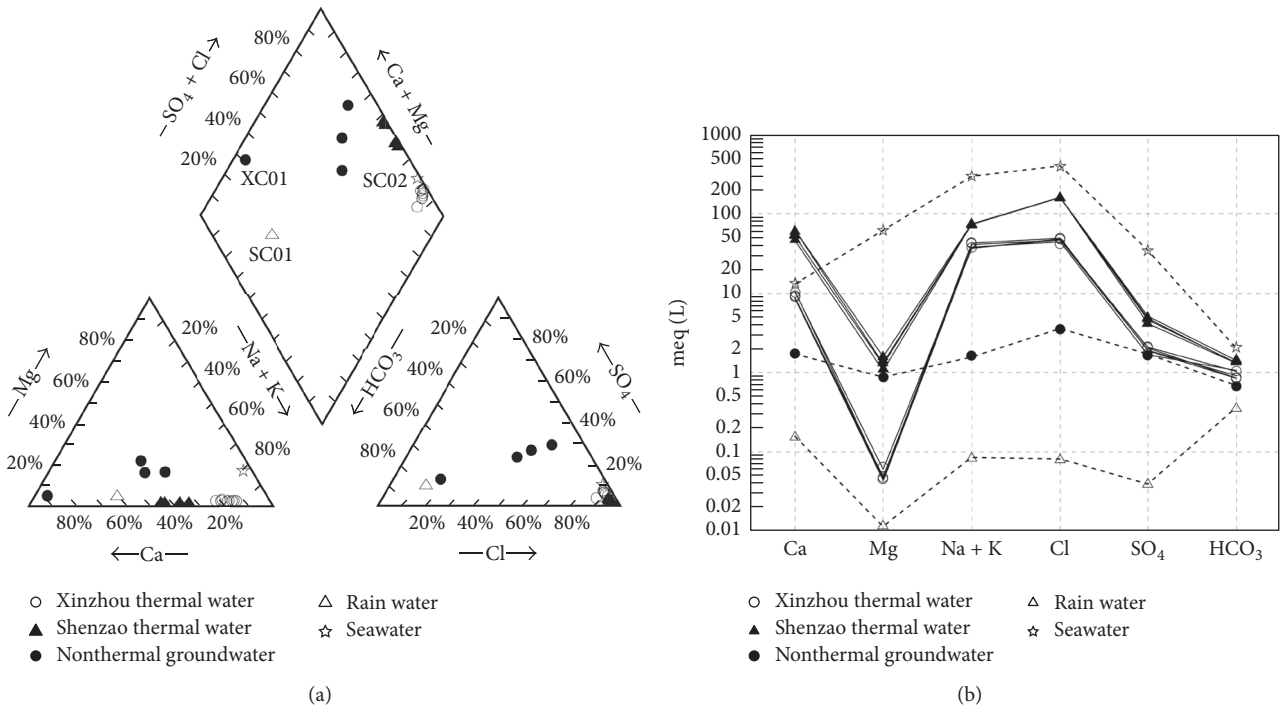


Figure 3: Distribution of thermal and nonthermal waters from the Xinzhou and Shenzao geothermal fields in Piper diagram (a) and Schoeller semilogarithmic diagram (b).

are higher (5.18 mg/L), compared with geothermal waters. For the geothermal water samples, Xinzhou and Shenzao have pH 8.13 and 7.60 on average, respectively. Flow temperature measured at the thermal drill outlets ranges from 70.75 to 98.30°C in Xinzhou and from 79.83 to 82.33°C in Shenzao. EC and TDS are significantly higher in Shenzao (means 14.46 mS/cm and 9254.50 mg/L, resp.) than in Xinzhou (means 4.59 mS/cm and 2251.59 mg/L, resp.). Geothermal water samples from both fields have very low negative oxidation-reduction potential (ORP) values ranging from −115 to −187 mV in Xinzhou field and from −93 to −132 mV in the Shenzao field. The negative ORP values observed in the geothermal waters probably result from loss of dissolved oxygen during the convection of fluids and are indicative of a reducing environment at depth [33]. The oxidation of sulfide (in $H_2S$) present in alkali chloride waters which forms bisulfate ($HSO_4$) during buffer action and neutralization of the wall rocks may also be involved in the development of this reducing condition [34]. Geothermal waters contain significantly lower DO concentrations at Xinzhou (2.83–4.55 mg/L) than those at Shenzao (4.10–5.23 mg/L). This contrast is likely because oxygen dissolved in water becomes less soluble as the temperature increases.

*4.1.2. Hydrogeochemical Characteristics.* Although most geothermal reservoirs are located at great depth, with no visible surface manifestation, geothermal energy can find its way to the surface in the form of hot springs, driven by buoyancy resulting from elevated temperature [35]. Thermal water resources originating from a fractured granite reservoir are related to deep, regional flow systems, characterized by long flow paths and extremely slow rates of groundwater movement [36]. At this regional scale, conventional hydrogeological investigations and numerical models of thermal water flow in a fractured granite aquifer have difficulty providing an adequate hydrogeological description due to the strong geological heterogeneities and multiple processes [37]. In such cases, basic research on the formation and geochemical evolution of thermal waters, involving sources of recharge, flow paths, mixing, and water-rock interaction processes, can provide scientific information to understand the heating mechanisms and groundwater flow systems in the geothermal system [38].

The hydrochemical characteristics based on physicochemical data of water samples in the study area are presented in Table 2. Thermal water samples comprise two relatively similar hydrochemical types, Na-Cl and Ca-Na-Cl types. Cold groundwater samples are mostly Ca-$HCO_3$, Ca-Na-$HCO_3$-Cl, and Ca-Na-$SO_4$-Cl types, whereas rainwater and seawater samples are of Ca-Na-$HCO_3$ and Na-Cl types.

The major ion concentrations are plotted on a Piper diagram (Figure 3(a)). Xinzhou and Shenzao thermal waters have Cl and Na and Ca as the dominant ions, with Cl averaging at 1575 mg/L and 5722 mg/L, Na at 809 mg/L and 1662 mg/L, and Ca at 171 mg/L and 1078 mg/L, respectively. However, major anions (Cl and $SO_4$) and cations (Na, Ca, and K) in Shenzao samples are commonly higher in concentrations than those from Xinzhou, except for a few ions, such as $HCO_3$ and F. As shown in the Schoeller diagram (Figure 3(b)), thermal waters have hydrochemical signatures

Table 3: Concentrations of major chemical constituents of water samples from Xinzhou and Shenzao (in mg/L).

| Label | $Cl^-$ | $Br^-$ | $SO_4^{2-}$ | $HCO_3^-$ | $NO_3^-$ | Ca | K | Mg | Na | Si | B | Charge balance |
|---|---|---|---|---|---|---|---|---|---|---|---|---|
| *In Xinzhou geothermal field* | | | | | | | | | | | | |
| XH01 | 1735.73 | 11.28 | 106 | 67.27 | 1.12 | 186.19 | 64.61 | 1.42 | 776.02 | 94.87 | 0.4 | 6.77 |
| XH02 | 1680.05 | 8.93 | 97.68 | 62.79 | 10 | 198.03 | 70.42 | 0.54 | 919.42 | 97.5 | 0.43 | 1.83 |
| XH03 | 1777.47 | 7.75 | 97 | 52.32 | 2.19 | 197.12 | 67.92 | 0.73 | 776.48 | 100.53 | 0.28 | 6.7 |
| XH04 | 1790.72 | 7.13 | 90.13 | 50.83 | 8.7 | 208.04 | 72.9 | 0.58 | 950.99 | 96.51 | 0.42 | 1.09 |
| XH05 | 1450.4 | 7.8 | 87.45 | 67.27 | 6.56 | 150.03 | 64.22 | 0.58 | 807.44 | 93.84 | 0.38 | 1.01 |
| XH06 | 1210.33 | 8.05 | 76.81 | 62.79 | 7.19 | 130.56 | 56.83 | 0.86 | 738.69 | 87.63 | 0.33 | 4.77 |
| XH07 | 586.3 | 2.49 | 46.29 | 79.54 | 23.59 | 44.2 | 19.78 | 0.33 | 295.5 | 47.7 | 0.14 | 5.75 |
| XH08 | 1558.75 | 7.31 | 80.54 | 64.28 | 9.65 | 175.11 | 63.61 | 0.52 | 835.36 | 93.95 | 0.39 | 0.64 |
| XH09 | 1393.16 | 8.21 | 89.02 | 74.75 | 0.13 | 121.21 | 54.66 | 0.7 | 669.65 | 90 | 0.35 | 6.43 |
| XC01 | 30.09 | 0 | 28.48 | 174.91 | 24.7 | 66.4 | 2.27 | 1.9 | 3.88 | 8.74 | 0 | 1.96 |
| XC02 | 32.84 | 0 | 24.05 | 37 | 43.2 | 11.5 | 3.55 | 3.14 | 15.81 | 19.62 | 0.01 | 0.93 |
| XC03 | 112.84 | 0 | 80.88 | 89.7 | 89.79 | 42.01 | 16.38 | 9.54 | 35.47 | 23.76 | 0.02 | 1.85 |
| XC04 | 125.74 | 0 | 81.39 | 41.86 | 3.69 | 35.11 | 19.7 | 10.72 | 23.84 | 8.34 | 0.02 | 5.75 |
| *In Shenzao geothermal field* | | | | | | | | | | | | |
| SH01 | 5721.48 | 31.09 | 214.17 | 77.22 | 2.19 | 933.84 | 162.06 | 10.71 | 1770.86 | 79.59 | 0.66 | 7.79 |
| SH02 | 5535.63 | 22.83 | 227.17 | 77.79 | 4 | 1207.61 | 209.41 | 15.87 | 1646.81 | 87.22 | 0.73 | 3.25 |
| SH03 | 5900.65 | 23.89 | 243.78 | 85.73 | 1.18 | 1253.9 | 216.46 | 19.29 | 1642.66 | 89.41 | 0.73 | 5.48 |
| SH04 | 5729.92 | 27.5 | 199.91 | 79.43 | 3.76 | 918.21 | 159.94 | 12.65 | 1587.25 | 81.7 | 0.65 | 8.46 |
| SC01 | 2.87 | — | 1.9 | 21.59 | — | 3.16 | 0.42 | 0.14 | 1.74 | — | — | — |
| SC02 | 14245.91 | 121.27 | 1667.78 | 121.01 | — | 260.7 | 247.4 | 756 | 6575 | 9.15 | 1.39 | — |

Charge balance: (cations − anions)/(cations + anions).

very similar to that of seawater, that is, Na > (Ca + Mg + K) and Cl > ($HCO_3$ + $SO_4$), but with a greater relative abundance of Ca and a depleted Mg level. This fact indicates that mixing with seawater is probably one of the important processes and factors that affect the hydrochemistry of the geothermal waters. Due to mixing with less seawater but more groundwater, the geothermal waters from Shenzao are plotted at higher levels on the Schoeller diagram than those from Xinzhou, which is consistent with their coastal locality.

All the major ion concentrations except $HCO_3$ and Mg in thermal water samples are higher than those in cold groundwater (Table 3). This is likely related to the long-term deep circulation of geothermal water along the N-E fault system, which allows more extensive fluid-rock interactions. Concentrations of major ions also vary significantly in cold groundwaters at different locations, reflecting the mixing processes in various proportions occurring between the geothermal water and cold groundwater.

Chloride (Cl) can serve as a useful tracer for geochemical cycling in hydrothermal systems because of its relatively conservative nature [5, 39]. Some major ions are well correlated against Cl for different water samples (Figure 4). The high positive Na versus Cl and K versus Cl correlations ($R^2$ = 0.96 and 0.95, resp.) in the thermal waters corroborate the conclusion that Cl contents arise from the contribution of seawater. Similarly, a hypothetical mixing line between fresh water and seawater end members which reflects the apparent mixing trend is also observed in the positive correlation plots of B, Br, and $SO_4$ versus Cl ($R^2$ = 0.71–0.89). Also, a good correlation between EC and Cl is also found ($R^2$ = 0.93), indicating mixing of thermal and nonthermal waters in upflow zones, which leads to the formation of intermediate thermal waters [40]. However, there is a poor negative correlation between Cl and $HCO_3$ in Xinzhou thermal waters, indicating that the concentrations of $HCO_3$ decrease with increasing Cl concentrations through the contribution of seawater. Meanwhile, the Xinzhou thermal waters show a similar variation with nongeothermal water, whereas the Shenzao samples cluster together in these plots, suggesting different evolutionary processes.

The compositional variation in geothermal waters is also strongly affected by local fluid-rock interactions concerning the contribution of seawater, as suggested by the spread of samples in the correlation plots of some minor ions against Cl. The relationships between Ca and Mg and Cl in thermal waters are probably due to the precipitation and dissolution of specific hydrothermal alteration minerals. Enrichment of Ca in thermal waters can be attributed to cation exchange processes between geothermal fluids and silicate minerals such as calcium-rich plagioclase feldspar [41]. In high-temperature thermal systems, Mg is incorporated into secondary alteration minerals by ion exchange reactions, resulting in very low Mg levels [42]. Intensive chloritization of the metasomatic biotite is observed in the Xinzhou 1000 m drill cores, and chloritization is an essential process in which Mg-rich chlorite is produced. Such a feature strongly suggests that the Mg exchange reactions make important contributions to the depletion of Mg in thermal waters.

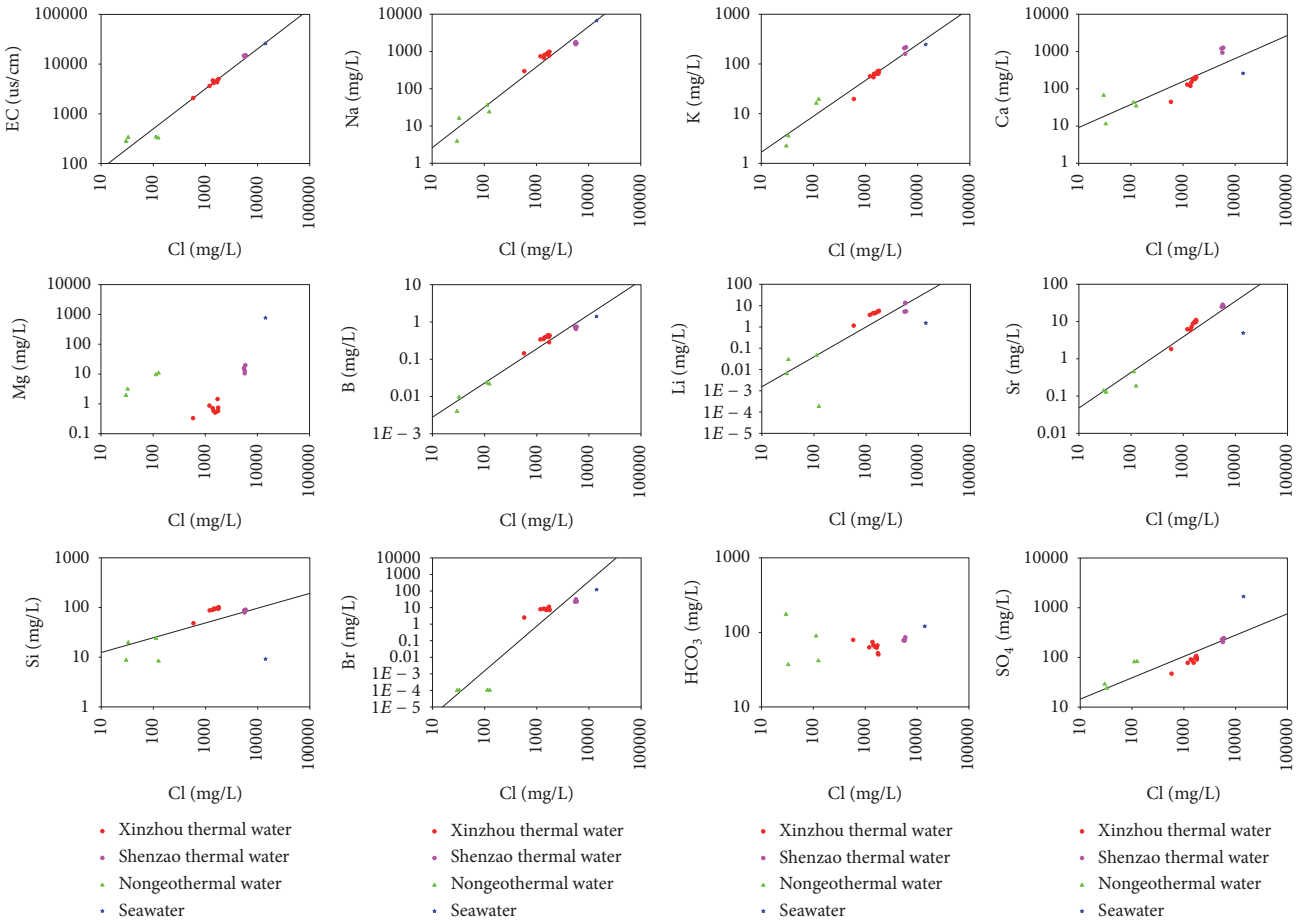


FIGURE 4: Relations between various ions (EC, Na, K, Ca, Mg, B, Li, Sr, Si, Br, $HCO_3$, and $SO_4$) and chloride for Xinzhou and Shenzao thermal and cold waters.

*4.1.3. Trace Elements.* Trace elements release from the water-rock interactions during groundwater circulation. General geothermal waters are more abundant in trace elements than cold groundwater, resulting from enhanced reaction rates or capacity under high temperature and high pressure.

In the study area, those elements, Li, Rb, Cs, Sr, and F, are much enriched in thermal waters than in cold groundwater (Table 4). Certain enrichment in thermal water is observed for Ba, Cr, Cu, and Mo. Moreover, no variation is noted for other elements (such as Pb, Sn, Zn, and Zr).

The concentrations of Li, Rb, Cs, and Sr in thermal waters are much higher than those of seawater, indicating that seawater is not the primary source for these elements. The excellent linear relationships between these elements and Cl (Figure 4) show evidence for mixing between cold groundwater and a geothermal fluid with Li, Rb, Cs, and Sr as characteristic constituents. The differences in the correlation plots can be attributed to geochemical processes along deep regional flow paths, in which thermal water approaches chemical equilibrium with different host rock types at different subsurface temperatures [43].

Dissolution of country rocks mainly controls the trace element in thermal waters. The intrusion rocks are dominantly biotite granite in the study area. And the biotite is the major Li-bearing mineral, while Rb and Cs reside in K-containing silica minerals [44]. It is clear that Li, Rb, and Cs are concentrated in biotite, which contains an order of magnitude more Li than the whole rock. Sr has a similar property to K and Ca and thus can be found in K- and Ca-rich minerals such as sulfate, carbonate, and feldspar [45]. These minerals provide the primary source of Li, Rb, Cs, and Sr for the geothermal waters.

The geothermal waters are relatively high in F contents from 230 to 3530 $\mu$g/L, second only to Sr. The F contents vary much for various geothermal waters, with the F contents in Shenzao thermal waters being significantly lower than those for Xinzhou. This can be explained by the equilibration with calcite and fluorite. As discussed later in Section 4.3.1, saturation index for selected minerals suggests that most of the thermal water samples are oversaturated with calcite and undersaturated with fluorite. Calcite precipitation leads to the removal of $Ca^{2+}$ from thermal waters, thus allowing more fluorite to dissolve [46].

Temperatures play a dominant role in controlling the release of trace elements, in addition to main control of lithological properties. From thermal dynamic prospect, the dissolution rates of silica minerals are significantly enhanced, while the source minerals of the trace elements in granite

Table 4: Trace element concentrations (in ppb) in the thermal and nonthermal water samples from Xinzhou and Shenzao.

| Label | Ba | Cr | Cs | Cu | F | Li | Mo | Pb | Rb | Sn | Sr | Zn | Zr |
|---|---|---|---|---|---|---|---|---|---|---|---|---|---|
| *In Xinzhou geothermal field* | | | | | | | | | | | | | |
| XH01 | 92.4 | 8.16 | 300 | 9.53 | 2430 | 1546 | 3.5 | 0.41 | 486 | 0.62 | 7256 | 23.9 | 0.1 |
| XH02 | 86.2 | 16 | 300 | 9.37 | 660 | 1618 | 3.69 | 0.21 | 494 | 0.13 | 7341 | 16.7 | 0.079 |
| XH03 | 68.8 | 16.5 | 270 | 8.42 | 500 | 1501 | 4.59 | 0.31 | 441 | 0.054 | 6300 | 19.9 | 0.031 |
| XH04 | 90.2 | 6.93 | 291 | 12.8 | 3530 | 1657 | 3.8 | 0.21 | 508 | 0.048 | 7197 | 3.87 | 0.018 |
| XH05 | 146 | 6.41 | 272 | 12.1 | 3460 | 1606 | 4.15 | 0.23 | 476 | 0.038 | 6617 | 3.62 | 0.017 |
| XH06 | 99.2 | 1.75 | 279 | 12.5 | 3490 | 1656 | 3.74 | 0.19 | 496 | 0.027 | 7105 | 2.24 | 0.025 |
| XH07 | 63.8 | 3.56 | 223 | 9.99 | 3420 | 1465 | 4.04 | 0.23 | 419 | 0.037 | 4428 | 2.16 | 0.017 |
| XH08 | 92.2 | 3.87 | 235 | 10.8 | 3500 | 1576 | 3.98 | 0.2 | 436 | 0.041 | 4916 | 3.51 | 0.013 |
| XH09 | 136 | 3.93 | 232 | 10.7 | 3780 | 1505 | 3.94 | 1.27 | 433 | 0.048 | 4292 | 54.8 | 0.017 |
| XC01 | 61.7 | 1.82 | 1.25 | 1.17 | 0 | 0.9 | 0.097 | 0.094 | 40.4 | 2 | 107 | 25 | 0.0041 |
| XC02 | 141 | 0.87 | 1.26 | 0.87 | 180 | 4 | 0.033 | 0.53 | 11.4 | 0.029 | 56.8 | 6.51 | 0.011 |
| XC03 | 45 | 0.45 | 0.5 | 0.67 | 220 | 29.2 | 0.41 | 0.093 | 3.77 | 0.019 | 98.6 | 4.91 | 0.011 |
| XC04 | 60.9 | 1.02 | 7.98 | 1.56 | 260 | 60.5 | 0.1 | 0.12 | 26.6 | 0.052 | 478 | 16.3 | 0.014 |
| *In Shenzao geothermal field* | | | | | | | | | | | | | |
| SH01 | 509 | 23.3 | 610 | 26.8 | 230 | 2920 | 1.6 | 0.86 | 1197 | 0.05 | 20656 | 16 | 0.31 |
| SH02 | 486 | 16.2 | 603 | 26.9 | 420 | 2914 | 1.57 | 0.13 | 1204 | 0.074 | 19820 | 19.4 | 0.099 |

vary in solubility, resulting in complex relations to water temperatures for various trace elements. The contents of Sr, Li, Rb, and Cs are correlated favorably with temperatures (Figure 5). Such a feature strongly suggests that water-rock interactions make important contributions to geothermal water chemistry, especially for the selected trace elements contents.

Br-Cl ratios are often used for analyzing the sources of salinity in groundwater, especially in the coastal area [47, 48]. The three lines in Figure 6 define if those Cl-rich thermal waters are genetically related to recent unmodified seawater, to residual ancient seawater, or to nonmarine rock salt. As shown in Figure 6, all the saline thermal water samples fall on or close to the unmodified seawater dilution line, suggesting that mixing with seawater is the important process controlling the chemistry of these samples. This mixing process with seawater for thermal water samples might be related to seawater in loose sediments of the coastal area and widespread deep faults in granite rocks [11].

*4.1.4. $\delta^{18}O$ and $\delta^{2}H$ Isotopes.* The stable isotopic ratios $\delta^{2}H$ and $\delta^{18}O$ of waters can be used for tracing the origin of geothermal fluids and estimating their recharge elevations [49]. The $\delta^{2}H$ and $\delta^{18}O$ isotopic values (versus SMOW) of thermal water samples are presented in Table 5. In addition, some isotopic data collected from previous studies are included for further analysis [11]. The isotopic composition of thermal waters shows narrow ranges of variation, with $\delta^{18}O$ and $\delta^{2}H$ ranging from −7.42‰ (XH07) to −4.99‰ (SH02) and from −46.5‰ (XH08) to −33.84‰ (SH02), respectively. The $\delta^{18}O$ and $\delta^{2}H$ values of Xinzhou thermal waters (−6.29‰ and −41.06‰ on average, resp.) are significantly lower than those of Shenzao thermal waters (−5.67‰ and −36.01‰ on average, resp.).

The relationships between the $\delta^{2}H$ and $\delta^{18}O$ values for the thermal and cold waters are plotted in Figure 7(a), in comparison with the Global Meteoric Water Line (GMWL; $\delta^{2}H = 8\delta^{18}O + 10$; Craig 1961 [50]) and the Local Meteoric Water Line (LMWL; $\delta^{2}H = 8.1\delta^{18}O + 11.4$; Yuan et al. 2013 [11]). All the thermal waters, as well as the cold groundwaters, are located around the local and global meteoric water lines, indicating that precipitation is the common origin of recharges, despite the extremely high salinity. Figure 7(a) also shows that the thermal waters are depleted in deuterium with low *d*-excess values ranging between 7.22 and 9.79‰ and deviate from the LMWL but are closely aligned along the mixing line, indicating that these waters initiated as paleometeoric water that flushed and mixed with seawater. It is noticeable that the $\delta^{2}H$ and $\delta^{18}O$ values of thermal waters can be divided into two distinct groups. This might be due to the high mixing ratios with seawater for Shenzao thermal waters.

A slight positive $\delta^{18}O$-shift in geothermal water samples is interpreted as the result of oxygen isotope exchange during long periods of fluid-rock interactions at high temperatures. The amount of oxygen exchange depends strongly on the reservoir temperature, residence time, and rock compositions [51]. In contrast, shifts in $\delta^{2}H$ do not take place because of the extremely small amount of hydrogen in reservoir rocks [52]. Therefore, the increases in $\delta^{2}H$ values are directly related to the contribution of seawater. However, the relatively high $\delta^{18}O$ values for cold groundwater compared to geothermal water imply a low-elevation recharge and a shallow circulation path.

The recharge elevations of groundwater can be estimated based on the altitude effect of stable isotope using

$$H = H_g + \frac{\left(D_p - D_g\right)}{\text{grad } D}, \quad (1)$$

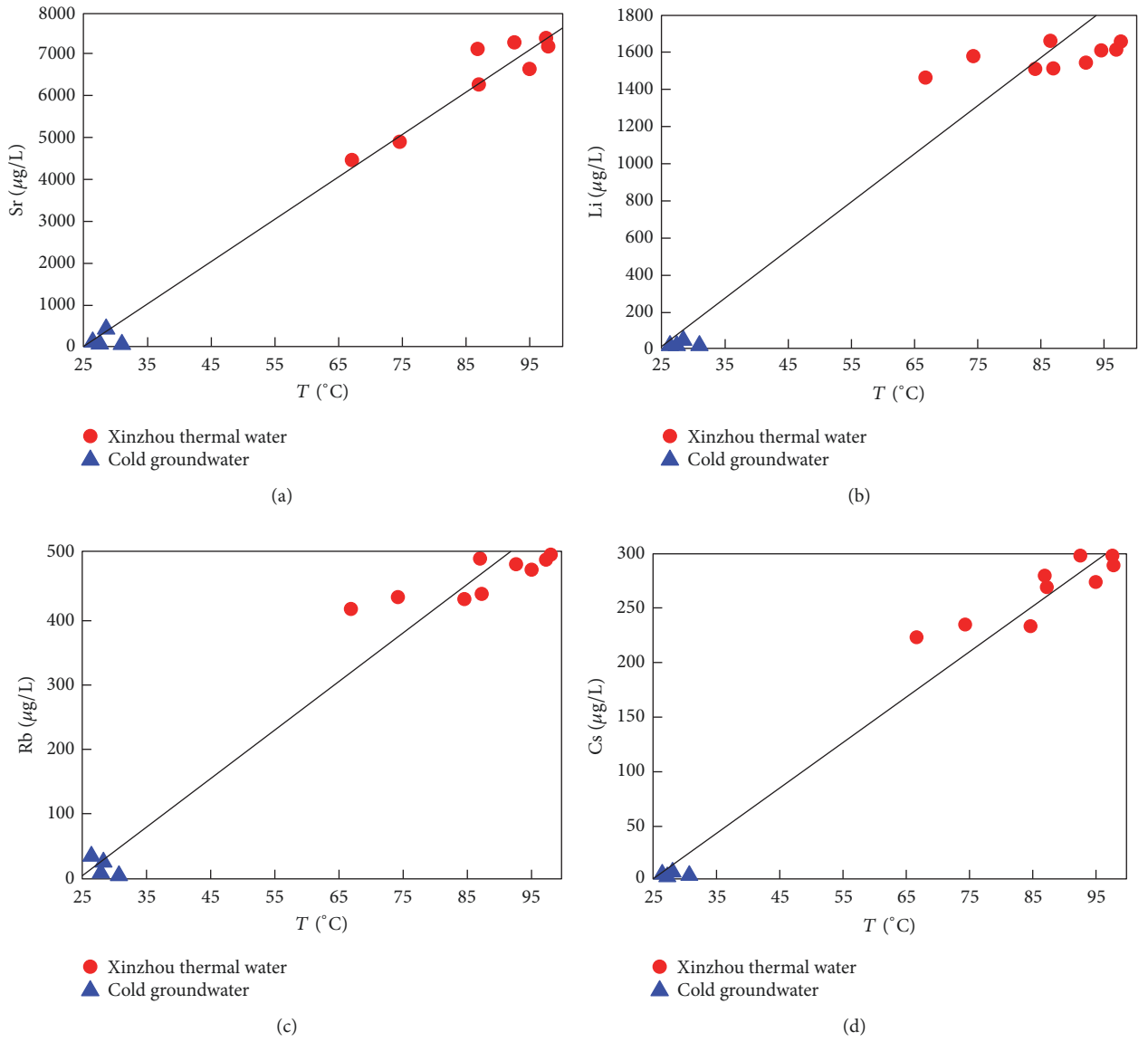


Figure 5: Correlation plots of (a) Sr, (b) Li, (c) Rb, and (d) Cs against temperature for the groundwater samples from Xinzhou and Shenzao areas.

where $H$ and $H_g$ are the altitude of groundwater recharge area and sampling sites (m.a.s.l.), respectively; $D_g$ and $D_p$ are the $\delta^2$H value of groundwater sample and precipitation near the sampling sites (‰), respectively; grad $D$ is the altitude-$\delta^2$H gradient in the study area (‰/m) [11]. The altitude-$\delta^2$H gradient in this region reported by Yuan et al., that is, −2‰/100 m, was used in (1) for calculation. The results showed that a mean recharge elevation of thermal water for Shenzao is 1184 m.a.s.l. higher than Xinzhou, which is 843 m.a.s.l. The recharge areas of the Xinzhou and Shenzao thermal waters are proposed to be located near the eastern Ziluo Mountain (~793 m.a.s.l.) and the northern piedmont of Dama Mountain (~1140 m.a.s.l.), respectively, which correspond to the inferred elevations for the recharge of meteoric water.

*4.2. Mixing Model.* Based on a solute mass-balance model, a conservative mixing line between fresh water and seawater end members for distinct isotopic compositions has been constructed to calculate the relative fractional contribution of the two hypothetical end members in mixed waters, utilizing the following general binary mixing equation:

$$\delta_m = \delta_s \times f + \delta_f \times (1 - f), \quad (2)$$

where $f$ is the fraction of the seawater in the mixture; $\delta_m$ is the isotopic tracer value of the mixture; $\delta_f$ is the isotopic tracer value of the fresh water; and $\delta_s$ is the isotopic value of the seawater. Figures 7(b) and 7(c) show the strong linear relationships in the $\delta^2$H versus Cl and $\delta^{18}$O versus Cl plots (with squared regression coefficients of 0.98 and 0.92, resp.),

Table 5: Stable isotopic compositions and calculated recharge elevations of thermal water samples from Xinzhou and Shenzao.

| Label | Name | Type | 2013 | | 2014 | | Evaluated recharge ele. (m.a.s.l.) |
|---|---|---|---|---|---|---|---|
| | | | $\delta$D (‰ SMOW) | $\delta^{18}$O (‰ SMOW) | $\delta$D (‰ SMOW) | $\delta^{18}$O (‰ SMOW) | |
| *In Xinzhou geothermal field* | | | | | | | |
| XH01 | New hole | TD | −41.5 | −6.2 | −39.0[a] | −6.4[a] | 942 |
| XH02 | Dun | TD | −43.0[a] | −6.4[a] | −41.2 | −6.2 | 872 |
| XH03 | Ta | TD | −44.0[a] | −6.5[a] | −41.1 | −6.2 | 833 |
| XH04 | Jia | TD | −41.0[a] | −6.7[a] | −41.6 | −6.5 | 970 |
| XH05 | Dongwei | TD | −43.2 | −6.5 | −44.0[a] | −6.8[a] | 855 |
| XH07 | Old hole | TD | −46.0[a] | −7.4[a] | −47.2[a] | −7.3[a] | 724 |
| XH08 | Xiting | TD | −46.5[a] | −7.2[a] | −42.1 | −6.7 | 704 |
| XC01 | Shanbian | AW | −42.6 | −6.4 | −39.8 | −5.8 | — |
| XC02 | Cunjin | AW | −42.8 | −6.5 | −44.0 | −5.8 | — |
| XC03 | Huangquan | AW | −41.4 | −6.1 | −41.6 | −5.5 | — |
| XC04 | Weijin | AW | −41.2 | −6.2 | −38.6 | −6.1 | — |
| *In Shenzao geothermal field* | | | | | | | |
| SH01 | Shenan | TD | −37.7 | −5.9 | −36.4 | −6.0 | 1198 |
| SH02 | Shenzhong | TD | −33.8 | −5.0 | −36.1 | −5.8 | 1216 |
| SH03 | Shenli | TD | −35.3 | −5.3 | −36.9 | −5.9 | 1168 |
| SH04 | Shenhai | TD | −34.9 | −5.4 | −37.1 | −6.0 | 1155 |
| SC01 | Haiyan | RF | — | — | −60.1 | −8.4 | — |

TD, thermal drill; AW, agricultural well; RF, rainfall; —, not applicable. [a]Previous data by Yuan et al. (2013).

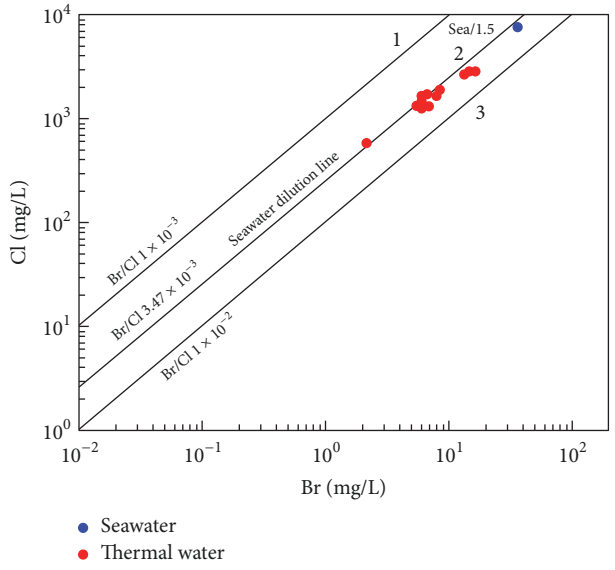


Figure 6: Bromide/chloride relationships in thermal waters relative to Br/Cl ratio in seawater. Dilution lines with nonmarine salt rock, fresh seawater, and residual ancient seawater are shown.

which demonstrates that the $\delta^2$H and $\delta^{18}$O values in thermal waters vary systematically with the relative mixing ratios of end members. In addition, a more sophisticated multiple end-member mixing model of dilution can be found in Lu et al.'s work [53].

The results of the mixing calculations for thermal waters are given in Table 6. Calculations were performed using both $\delta^{18}$O and $\delta^2$H, so that for each tracer there is a different $f$ value. The results of calculating seawater fractions are broadly consistent between the two isotopic tracers ($\delta^2$H and $\delta^{18}$O), accounting for associated uncertainties in measurement. Nevertheless, the samples are divided into two well-defined groups: those from Xinzhou, for which $\delta^{18}$O yields a larger $f$ value (average difference of 6.66%), and those from Shenzao, for which $\delta^2$H produces a slightly larger $f$ value (average difference of 4.61%). This result is likely related to much more extensive deep circulation of thermal water at Xinzhou, which has undergone an increase in $\delta^{18}$O from sources other than the mixing of end members, such as large-scale oxygen isotope exchange during high-temperature fluid-rock interactions. Due to the small amount of hydrogen in rocks, the $\delta^2$H values are chosen as a relatively conservative tracer to characterize the mixing process.

The interpretation of the isotopic data for thermal waters through the mixing model suggests the occurrence of extensive subsurface seawater intrusion into the Xinzhou and Shenzao geothermal fields (average percentages of seawater are 18.92% and 42.02%, resp.). Due to proximity to the coast, it is clear that Shenzao field exhibits much higher proportions of seawater within the thermal water than those of Xinzhou. This is favored by the wide distribution of underlying impermeable granites.

Xinzhou is 10 km inland from the coastline along the major NE-striking deep faults and thermal waters display

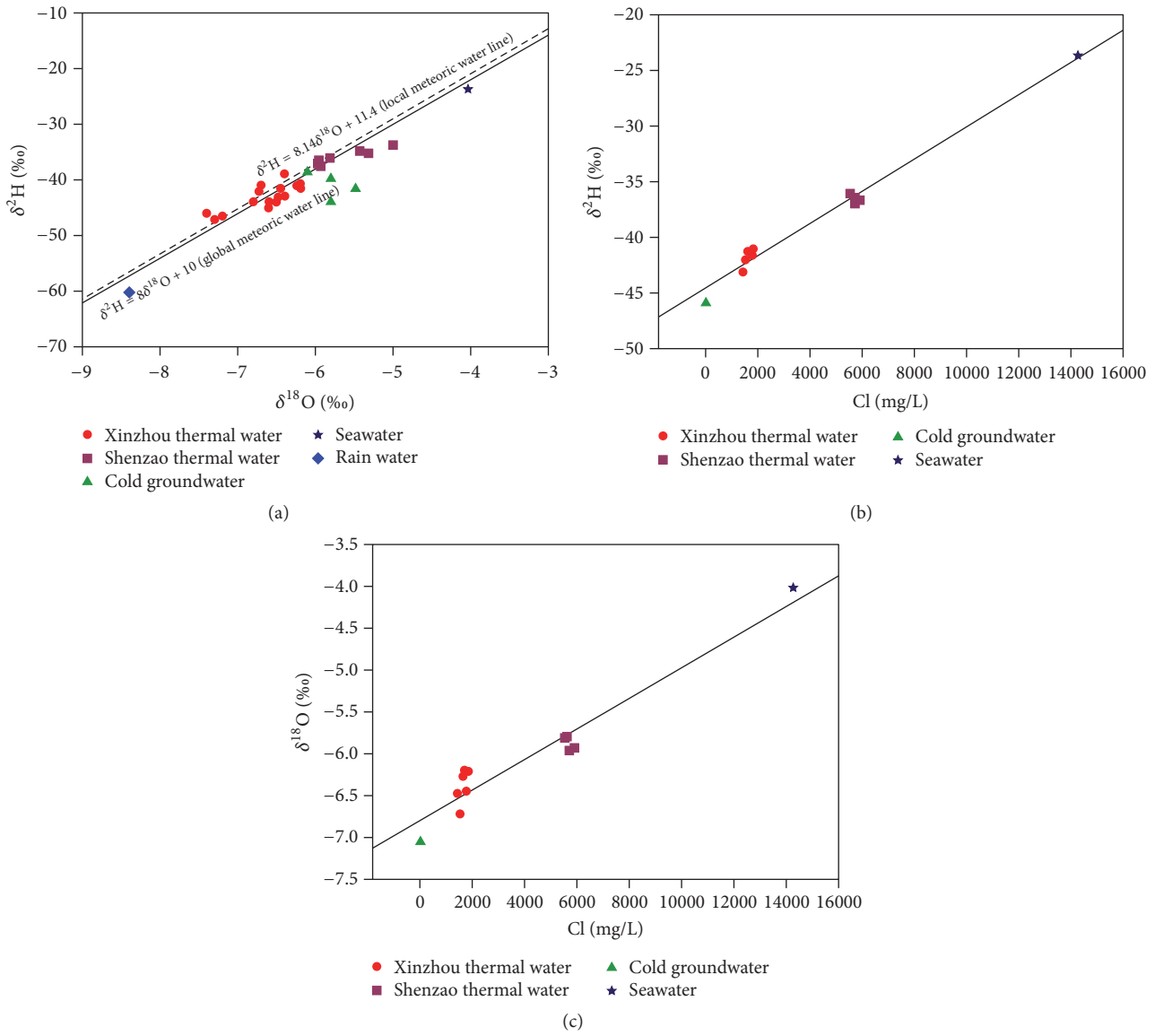


Figure 7: (a) Relationship of $\delta^{18}$O and $\delta^2$H in groundwater with the GMWL and LMWL at Xinzhou and Shenzao; (b) $\delta^2$H-Cl diagram; and (c) $\delta^{18}$O-Cl diagram.

slightly lower salinity, indicating a deep circulation of seawater. Seawater might infiltrate through granite fractures to enter the hydrothermal system. Once it penetrates into the underlying Yanshanian basement rocks, the chemical composition of trapped seawater is constantly altered by both mixing processes and water-rock interactions during a relatively long-term migration until equilibrium is reached. As a result, the interaction of granite with diluted seawater in the geothermal reservoir could produce a slightly saline geothermal fluid that is depleted in Mg and highly enriched in $SiO_2$ (Figure 4). During its migration upward to the land surface along the deep fault, driven by buoyancy, the input of chemical compositions from rivers could also contribute to this alteration. The Shouchang River appears to be an important source of recharge for Well XH05, which exhibits the lowest seawater fraction at 12.42% and the most depleted isotopic composition found within the thermal water.

### 4.3. Equilibrium Status of Geothermal Water

*4.3.1. Mineral Saturation States.* Mineral equilibrium calculations were performed to determine the potentially reactive minerals and estimate the activity coefficients of dissolved species in hydrothermal systems. The saturation index (SI), a measure of a solution's ability to dissolve or deposit relevant minerals, was used to evaluate the degree of fluid-mineral equilibrium. The USGS computer program PHREEQC [54] was used to calculate saturation indices of potential minerals with respect to the given hydrochemical data at measured discharge temperatures for the two hydrothermal systems. In each system, the saturation indices of potentially relevant

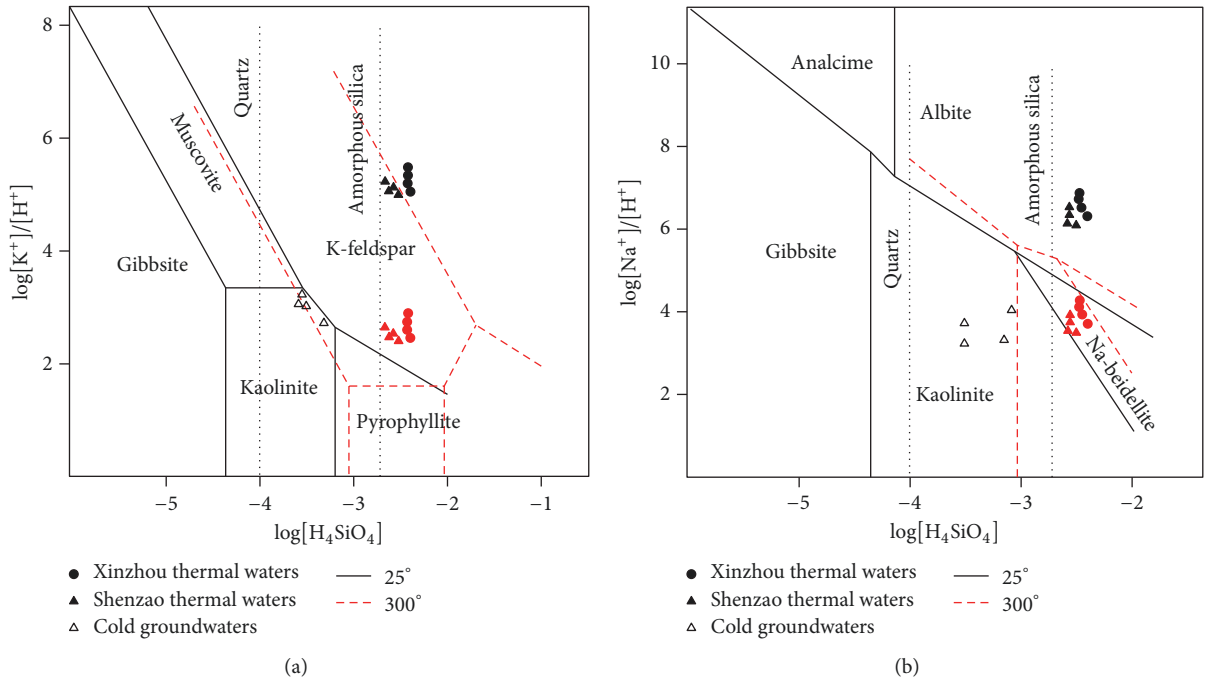


Figure 8: Stability diagrams for groundwater samples at 25°C and 300°C in the systems of (a) $K_2O$–$Al_2O_3$–$SiO_2$–$H_2O$ and (b) $Na_2O$–$Al_2O_3$–$SiO_2$–$H_2O$ from the Xinzhou and Shenzao geothermal fields.

Table 6: Fresh water and seawater percentages in thermal waters from Xinzhou and Shenzao geothermal fields.

| Label | Name | Type | Based on $\delta^{18}O$ | | Based on $\delta^{2}H$ | |
|---|---|---|---|---|---|---|
| | | | $f_{fw}$ (%) | $f_{sw}$ (%) | $f_{fw}$ (%) | $f_{sw}$ (%) |
| *In Xinzhou geothermal field* | | | | | | |
| XH01 | New hole | TD | 71.52% | 28.48% | 79.79% | 20.21% |
| XH02 | Dun | TD | 72.85% | 27.15% | 78.40% | 21.60% |
| XH03 | Ta | TD | 71.85% | 28.15% | 77.95% | 22.05% |
| XH04 | Jia | TD | 80.13% | 19.87% | 80.24% | 19.76% |
| XH05 | Dongwei | TD | 80.79% | 19.21% | 87.58% | 12.42% |
| XH08 | Xiting | TD | 89.07% | 10.93% | 82.49% | 17.51% |
| XC01 | Shanbian | AW | 100.00% | 0.00% | 100.00% | 0.00% |
| *In Shenzao geothermal field* | | | | | | |
| SH01 | Shenan | TD | 63.91% | 36.09% | 57.16% | 42.84% |
| SH02 | Shenzhong | TD | 58.94% | 41.06% | 55.67% | 44.33% |
| SH03 | Shenli | TD | 63.25% | 36.75% | 59.05% | 40.95% |
| SH04 | Shenhai | TD | 64.24% | 35.76% | 60.04% | 39.96% |
| SC02 | Zhenhai | SW | 0.00% | 100.00% | 0.00% | 100.00% |

Samples SC02 (seawater) and XC01 (cold fresh water) accepted as the end members of the mixing. TD, thermal drill; AW, agricultural well; RF, rainfall; SW, seawater; $f_{fw}$, the fraction of fresh water; $f_{sw}$, the fraction of seawater.

minerals—carbonate (calcite, aragonite, and dolomite), sulfate (gypsum, anhydrite, and celestite), and silica (quartz and chalcedony)—are listed (Table 7).

The results show that all the thermal waters are undersaturated with respect to anhydrite and gypsum, indicating that dissolution of sulfate is an ongoing process. Most are oversaturated or nearly in equilibrium with respect to aragonite, calcite, chalcedony, dolomite, and quartz, indicating that precipitation of carbonate and silica minerals has evidently occurred. Fluorite is another mineral that reaches equilibrium with the Shenzao thermal waters. Unlike carbonate, the tendency of the fluorite activity product to reach the equilibrium value is driven by increasing electrical conductivity rather than temperature [55]. On this basis, we

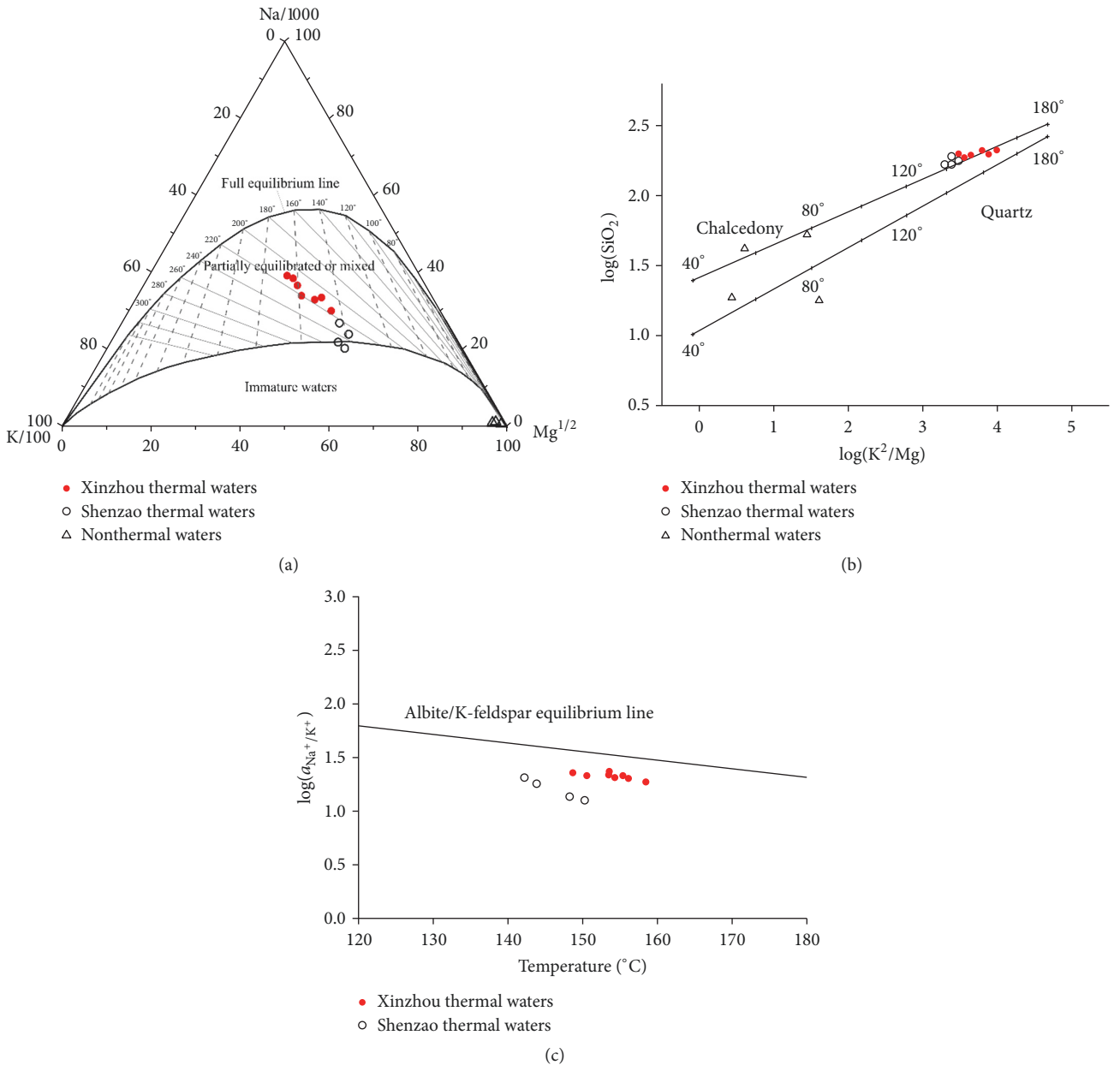


FIGURE 9: Applicability of geothermometers for thermal and nonthermal samples from the Xinzhou and Shenzao geothermal fields. (a) Na–K–Mg triangular diagram; (b) $SiO_2$ versus $K^2/Mg$ ratio. Lines indicate the temperature dependence of the variables for minerals and (c) nonequilibrium indicated by the Na/K activity ratio in the predicted chalcedony temperature range.

assume that fluorite's undersaturation in the Xinzhou thermal water is closely related to dilution by fresh groundwater flow, which leads to a decrease in electrical conductivity. These findings show that a potential scale deposition of aragonite, calcite, dolomite, and quartz occurred in both the Xinzhou and Shenzao geothermal fields, which is consistent with the lack of gypsum and anhydrite in sandstone and carbonate-rock aquifers.

*4.3.2. Stability Diagrams of Silicate Minerals.* Stability diagrams (Figure 8) are constructed to portray the stability fields of aluminosilicates, which are predominant components of clay minerals in decomposed granite. During this process, 8 pure minerals, gibbsite, muscovite, kaolinite, K-feldspar, pyrophyllite, analcime, albite, and Na-beidellite, were taken into account to depict the phase stability relations in the $K_2O$–$Al_2O_3$–$SiO_2$–$H_2O$ and $Na_2O$–$Al_2O_3$–$SiO_2$–$H_2O$ systems. Reactivity trends with equilibrium constants ($K_{eq}$) of any reactions of these minerals were computed by the TOUGHREACT simulation program [56]. Since the mineral phase boundaries are dependent on the temperature conditions, the computations were performed at 25°C and 300°C to quantify the effects of temperature. The pH at an elevated temperature was calculated using corresponding

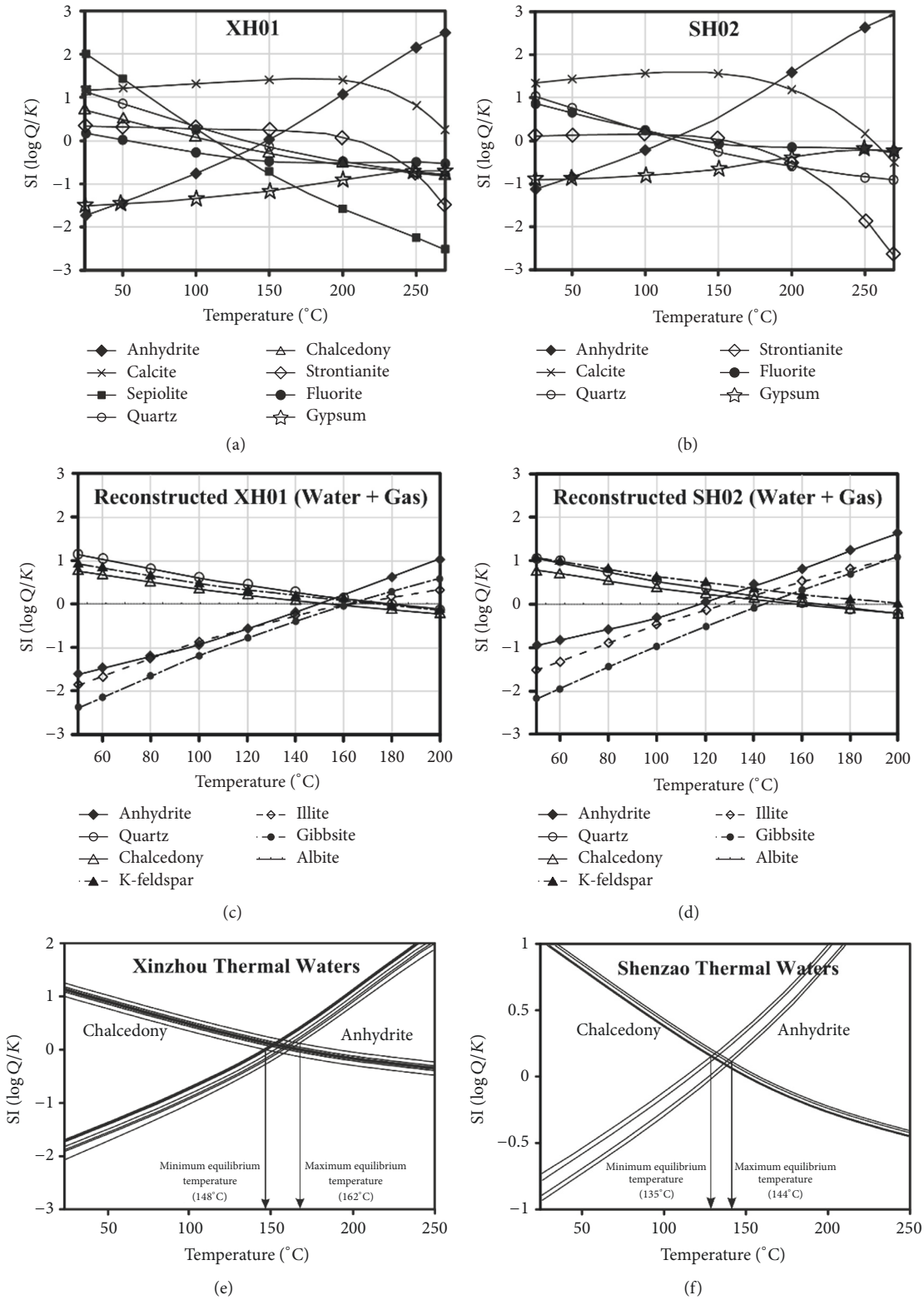


Figure 10: Multicomponent geothermometry using Xinzhou and Shenzao geothermal water. Top graphs ((a) and (b)): mineral equilibrium diagram for XH01 (a) and SH02 (b) as representatives of studied geothermal water; middle graphs ((c) and (d)): FixAl results for reconstructing mineral equilibria in XH01 (c) and SH02 (d), fixing the Al concentration by equilibrium with albite and a 100% CO2 gas add back; bottom graphs ((e) and (f)): result showing equilibrium temperature estimations for the Xinzhou (e) and Shenzao (f) thermal waters using the combination of anhydrite/chalcedony saturation indexes (modified from Pastorelli et al. [17]).

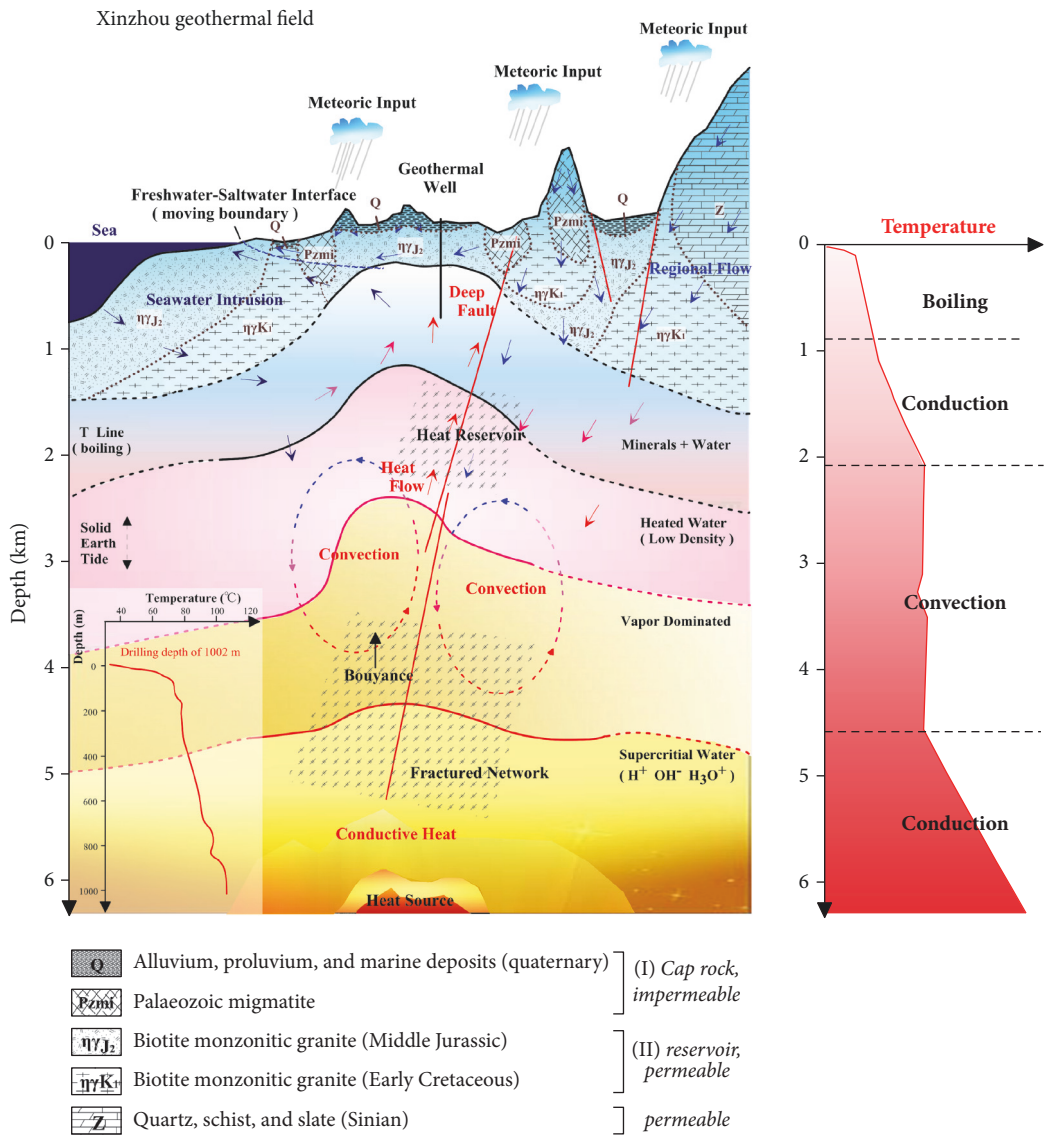


Figure 11: Schematic hydrogeological section showing the proposed circulation model of thermal groundwater in the coastal Xinzhou geothermal fields (blue to red arrows of "regional groundwater flow" indicate cold to hot water). Inset figures show the variation in temperatures versus monitoring depth. Bores show an increased geothermal gradient within the upper 0–200 m and a steady temperature gradient. The geothermal gradient remains constant within a range of 0.03–0.05°C/m below 400 m and down to the bottom, emphasizing the influence of the geothermal water.

water dissociation constants. This led the water chemistry to shift to a lower part of the figure.

The results show that typical cold groundwaters from the supergene zone are likely precipitating kaolinite, whereas thermal waters tend to precipitate both K-feldspar and albite. Meanwhile, thermal waters are supersaturated with all secondary minerals, which causes formation under a wide range of conditions. Note that thermal waters reaching the stable state for K-feldspar and albite have to undergo a long-term deep circulation through the host rocks to accumulate significant concentrations of $SiO_2$, which is favored by both the deep fault and the fractured rocks. The data also indicate that the thermal waters may reach saturation with respect to K-feldspar slightly before saturation with albite. It is also observed that the stability field boundaries shift toward the positive direction from the origin and a significant increase occurs in the stability fields of K-feldspar and albite with increasing temperature. This behavior is a consequence of the increase in the alteration potential of the hydrothermal solution as temperature increases and indicates that K-feldspar and albite are more stable at higher temperatures.

### 4.4. Geothermometry

*4.4.1. Chemical Geothermometers.* Temperatures in the subsurface reservoirs yielding the deep thermal waters, as a crucial parameter in geothermal exploration, can be estimated by several traditional chemical geothermometers, including

Na-K [57], K-Mg [25], Na-K-Ca [26], Na-K-Ca-Mg [58], Na-Li [27], chalcedony [23], and quartz [24]. This further aids in estimating the depth of groundwater circulation, based on an understanding of regional tectonics and geothermal gradients [33]. However, strict attention should be paid to the assumed conditions that must be satisfied for every thermal water sample when applying most geothermometers.

Different geothermometers were applied to the thermal waters of Xinzhou and Shenzao, and their results are given in Table 8. However, chemical processes (e.g., mixing and evaporation) affect reservoir temperature estimates. To get an accurate estimation, the reliability of these solute geothermometers was also evaluated by comparing the measured bottom-hole temperature (BHT) of the geothermal wells (Table 9). The following formula used for this comparison is developed by Pandarinath (2011) [59]:

$$\text{difference } (\%) = \frac{T_{\text{Geotherm}} - T_{\text{BHT}}}{T_{\text{BHT}}} \times 100, \quad (3)$$

where $T_{\text{Geotherm}}$ and $T_{\text{BHT}}$ are the reservoir temperature estimated by solute geothermometer and the average BHT of the geothermal wells, respectively. These difference percentages between the estimated reservoir temperature and BHT were used to find out whether the estimated reservoir temperatures are acceptable ($\leq \pm 20\%$), based on the total propagated errors quantified in some solute geothermometers [60].

It can be seen from Tables 8 and 9 that the predicted temperatures of the reservoir are much higher than the measured wellhead temperatures of geothermal waters and present the vast differences compared to the BHT. According to the silica geothermometers, the results of quartz geothermometer yield reservoir temperatures varying from 176 to 185°C for Xinzhou and from 169 to 177°C for Shenzao. Temperatures estimated by the chalcedony geothermometer are from 149 to 158°C for Xinzhou and from 142 to 150°C for Shenzao. Statistical comparison of the estimated reservoir temperatures indicates that the majority of the reservoir temperatures estimated by chalcedony have differences < 20% compared to the BHT. However, the temperature prediction performance by quartz is very poor. Also shown in the plot of log ($SiO_2$) versus log ($K^2$/Mg) (Figure 9(b)), data points of all geothermal waters approach the chalcedony line very closely, suggesting that chalcedony rather than quartz probably controls the dissolved silica content. In general, at temperatures of less than 180°C, the silica solubility is governed by chalcedony rather than quartz, as suggested by Fournier [23]. On the other hand, saturation indices (SIs) for chalcedony are very close to zero, indicating its equilibrium with geothermal fluids. Accordingly, the chalcedony geothermometer appears to produce more reasonable results than quartz.

Of the cation geothermometers applied to geothermal water, Na-K geothermometers give unexpectedly high temperatures ranging from 212 to 218°C for Xinzhou and from 225 to 255°C for Shenzao. None of the estimated temperatures by Na-K are within the acceptable differences. Although Na-K geothermometers readjust relatively slowly in mixing systems, which makes this geothermometer less sensitive to the secondary processes (e.g., mixing and boiling), this geothermometer may yield an overestimated result at lower temperature [38], which occurs because leaching processes rather than chemical equilibrium control the Na-K contents in geothermal water at lower reservoir temperatures. The application of Na-K geothermometers may also lead to unreasonably high-temperature estimates for waters having high Ca contents.

To eliminate the effects of high Ca contents on the Na-K geothermometer, the Na-K-Ca geothermometer developed by Fournier and Truesdell [26] was used. A plausible reservoir temperature estimate in the range from 143 to 150°C for Xinzhou and from 147 to 152°C for Shenzao can be obtained from this geothermometer. The success rates (acceptable differences; <20%) in predicting the reservoir temperatures by Na-K-Ca for Xinzhou and Shenzao thermal waters are, respectively, 88% and 50%. The effect of dilution is minimal since the geothermal water is much more saline than the diluting water. However, this geothermometer is strongly affected by the precipitation of calcite with the loss of carbon dioxide due to boiling.

Temperatures calculated by K-Mg geothermometers from thermal waters of Xinzhou and Shenzao are mostly in the range of 139–168°C. The estimated temperatures of Xinzhou have shown wide differences (>20%), whereas those of Shenzao are within 20% differences compared to the BHT. This geothermometer is usually used when dissolved Na and Ca are not in equilibrium with minerals [61]. Mg usually reflects equilibrium at shallower levels, and the K-Mg geothermometer is not a good indicator of deep temperatures. However, since thermal waters from Xinzhou and Shenzao have high contributions from seawater, this geothermometer gives more reliable results than the Na-K and Na-K-Ca geothermometers.

The Na-Li geothermometer [27] produces unexpectedly high temperatures ranging up to ~220°C, which seems too high for the reservoir temperature. Almost all of the estimated temperatures have differences > 20% when compared with the BHT. In low-enthalpy geothermal systems, the geothermometer appears to be sensitive to TDS and rock type. As Li is a relatively minor constituent and Na is a major constituent in the Xinzhou and Shenzao geothermal water, the Na-Li geothermometer is not adequately calibrated, and its reliability is low. Slight changes in Li can have a significant impact on the Na/Li ratios.

These subsurface temperatures are similar to those estimated by Yuan et al. (2013) [11] who concluded that the regional geothermal gradients are the primary heat source for the thermal waters in this region. Subsurface temperature measurements for this region compiled by Institute of Hydrogeology of Guangdong indicate that the average geothermal gradient is approximately 42°C/km and the highest measured temperature was about 148°C at a depth of 3050 m [16]. Therefore, most of the thermal waters from the study area acquire their temperatures due to heating of percolating groundwater through fractures in the high geothermal gradients. Xinzhou thermal waters have the highest wellhead temperatures as the result of the fault systems, which facilitate the rise of deep heat flow at those localities.

Table 7: Calculated saturation indices (SI) for thermal water samples from Xinzhou and Shenzao geothermal field.

| Sample name | Label | Temperature (°C) | Anhydrite | Aragonite | Calcite | Celestite | Chalcedony | Dolomite | Fluorite | Gypsum | Halite | Quartz | $SiO_2$(a) |
|---|---|---|---|---|---|---|---|---|---|---|---|---|---|
| Xinzhou thermal waters | XH01 | 95.10 | −1.01 | 0.99 | 1.10 | −0.78 | 0.06 | 0.28 | −0.37 | −1.42 | −4.70 | 0.31 | −0.59 |
| | XH02 | 94.60 | −1.04 | 0.93 | 1.03 | −0.82 | 0.08 | −0.28 | −0.29 | −1.44 | −4.64 | 0.33 | −0.57 |
| | XH03 | 97.50 | −0.99 | 0.96 | 1.06 | −0.74 | 0.04 | −0.16 | −0.42 | −1.42 | −4.69 | 0.29 | −0.60 |
| | XH04 | 98.30 | −1.01 | 0.94 | 1.04 | −0.80 | 0.01 | −0.32 | −0.45 | −1.46 | −4.61 | 0.25 | −0.63 |
| | XH05 | 70.75 | −1.50 | 0.67 | 0.79 | −1.13 | 0.27 | −0.38 | −0.17 | −1.63 | −4.70 | 0.58 | −0.44 |
| | XH06 | 59.45 | −1.72 | 0.74 | 0.86 | −1.25 | 0.33 | 0.05 | −0.21 | −1.73 | −4.79 | 0.66 | −0.41 |
| | XH07 | 81.10 | −1.90 | 0.69 | 0.80 | −1.67 | −0.13 | −0.14 | −0.97 | −2.14 | −5.49 | 0.15 | −0.81 |
| | XH08 | 87.00 | −1.27 | 0.98 | 1.09 | −0.99 | 0.11 | −0.04 | −0.39 | −1.57 | −4.69 | 0.38 | −0.56 |
| | XH09 | 79.20 | −1.44 | 0.95 | 1.06 | −1.11 | 0.15 | 0.27 | −0.42 | −1.65 | −4.81 | 0.44 | −0.53 |
| Shenzao thermal waters | SH01 | 81.42 | −0.64 | 0.86 | 0.97 | −0.55 | 0.14 | 0.40 | 0.00 | −0.89 | −3.89 | 0.42 | −0.54 |
| | SH02 | 82.33 | −0.54 | 1.22 | 1.33 | −0.62 | 0.16 | 1.16 | 0.37 | −0.80 | −3.94 | 0.44 | −0.51 |
| | SH03 | 79.83 | −0.54 | 1.17 | 1.28 | −0.59 | 0.20 | 1.17 | 0.43 | −0.77 | −3.91 | 0.48 | −0.48 |
| | SH04 | 81.23 | −0.67 | 1.17 | 1.28 | −0.56 | 0.14 | 1.09 | 0.07 | −0.92 | −3.93 | 0.42 | −0.54 |

Table 8: Reservoir temperatures (°C) estimated using selected geothermometers and reservoir depth.

| Label | Name | Wellhead temperature (°C) | Quartz, no steam loss, °C [23] | Quartz, °C [24] | Chalcedony, °C [23] | Na-K, °C [25] | Na-K-Ca, °C [26] | K-Mg, °C (Giggenbach et al., 1983) | Na–Li, °C [27] | Reservoir depth (km) |
|---|---|---|---|---|---|---|---|---|---|---|
| *In Xinzhou geothermal field* | | | | | | | | | | |
| XH01 | New hole | 95 | 181 | 182 | 154 | 218 | 143 | 148 | 219 | 3.55–4.10 |
| XH02 | Dun | 95 | 183 | 183 | 156 | 212 | 148 | 169 | 200 | 3.59–4.14 |
| XH03 | Ta | 98 | 185 | 186 | 158 | 222 | 144 | 161 | 229 | 3.64–4.20 |
| XH04 | Jia | 98 | 182 | 183 | 156 | 212 | 148 | 169 | 203 | 3.58–4.13 |
| XH05 | Dongwei | 71 | 180 | 181 | 154 | 215 | 150 | 164 | 198 | 3.54–4.08 |
| XH06 | Dongmao | 60 | 176 | 176 | 149 | 212 | 147 | 152 | 190 | 3.43–3.96 |
| XH08 | Xiting | 87 | 180 | 181 | 154 | 212 | 145 | 165 | 199 | 3.54–4.08 |
| XH09 | Dongtang | 79 | 178 | 178 | 151 | 217 | 146 | 154 | 214 | 3.47–4.00 |
| *In Shenzao geothermal field* | | | | | | | | | | |
| SH01 | Shenan | 81 | 169 | 170 | 142 | 225 | 149 | 143 | 227 | 3.29–3.80 |
| SH02 | Shenzhong | 82 | 175 | 176 | 148 | 252 | 152 | 145 | 150 | 3.43–3.95 |
| SH03 | Shenli | 80 | 177 | 177 | 150 | 255 | 152 | 142 | 151 | 3.46–3.99 |
| SH04 | Shenhai | 81 | 171 | 171 | 144 | 233 | 147 | 139 | 243 | 3.33–3.84 |

Table 9: The differences (in percentage) between the reservoir temperatures estimated by solute geothermometers for thermal waters and the average measured bottom-hole temperature (BHT[a]) of the geothermal wells.

| Geothermometer | Difference percentage between the estimated reservoir temperature and respective BHTs | | | | | |
|---|---|---|---|---|---|---|
| | In Xinzhou geothermal field | | | In Shenzao geothermal field | | |
| | 0–20% | 20%–30% | >30% | 0–20% | 20%–30% | >30% |
| Quartz, no steam loss [23] | 0 | 0 | 8 | 0 | 0 | 4 |
| Quartz [24] | 0 | 0 | 8 | 0 | 0 | 4 |
| Chalcedony [23] | 8 | 0 | 0 | 3 | 1 | 0 |
| Na-K [25] | 0 | 0 | 8 | 0 | 0 | 4 |
| Na-K-Ca [26] | 7 | 1 | 0 | 1 | 3 | 0 |
| K-Mg (Giggenbach et al., 1983) | 1 | 3 | 4 | 4 | 0 | 0 |
| Na–Li [27] | 0 | 0 | 8 | 0 | 0 | 4 |

[a]Average bottom-hole temperature (BHT) of 135°C for geothermal wells calculated from the compiled southwestern Guangdong geothermal wells database of the Geological Survey of Guangdong Province (1988).

However, the estimated temperatures by using solute geothermometers for Xinzhou and Shenzao thermal waters are enormously higher than the BHT. The occurrence of seawater intrusion appears to be probably a critical reason for the overestimated reservoir temperatures. Major constituents such as sodium, potassium, calcium, and magnesium ions of thermal water change considerably in the process of intrusion. Apart from this, the differences in lithology and pattern of seawater intrusion between the two geothermal systems can also result in the observed differences in the reservoir temperatures obtained by various geothermometers. Xu and Guo (2017) [62] have reported that a km-scale fault-induced seawater intrusion might infiltrate through the granite fractures to get into the underlying Yanshanian basement rocks and mix with ascending thermal waters at Xinzhou. The compositions of trapped seawater are continuously altered by both mixing process and water-rock interactions during a relatively long-term migration. For the thermal waters of Shenzao, the inflow of seawater that directly feeds thermal aquifers has been identified [63]. Due to proximity to the coast, seawater fingerprints can be seen locally in the alluvium deposits at Shenzao. The compositions of thermal water are strongly influenced by a tidally forced moving interface between saltwater and the fresh water and change cyclically under solid tidal waves.

To make a clear distinction for the suitability of thermal waters for the application of geothermometers, the Na/1000-K/100-Mg1/2 ternary diagram of Giggenbach [25] was applied to determine the equilibrium state of water samples (Figure 9(a)). This plot shows that all thermal water samples are far from the full equilibrium line and correspond to partially equilibrated water or mixing, suggesting that the complete chemical reequilibrium of geothermal water samples has not been achieved because of limited water-rock interactions under low temperature or mixing process. The plot of the Na/K activity ratio versus the chalcedony temperature (Figure 9(c)) also demonstrates that equilibrium with albite and K-feldspar is not reached in the thermal waters of Xinzhou and Shenzao. Overall, as the processes of seawater intrusion can seriously affect the cation concentrations and the nonequilibrium conditions, chalcedony geothermometers may provide more reliable results than other silica and cation geothermometers.

*4.4.2. Geothermometrical Modeling.* There is a different approach to provide temperature estimates based on the state of equilibrium between thermal water and many hydrothermal minerals. The application of multicomponent chemical equilibria calculations can be used to validate the varied estimated temperature results from different geothermometers [64–67]. Several additional processes (including mineral reequilibrium and mixing with cold water during upward flow) can also be ascertained by this approach [68].

Geothermometrical modeling calculations have been performed for thermal waters using the PHREEQC computer code. The saturation indices of the ten most common hydrothermal minerals were initially calculated at the discharge temperatures and measured pH values. Furthermore, to determine the equilibrium states at different temperatures, saturation indices were then recalculated taking into account the hydrogen mass balance.

Mineral equilibrium diagrams (Figures 10(a) and 10(b)) depict the mineral saturation indices versus increasing temperature. For the Xinzhou thermal waters, the saturation states with respect to quartz, chalcedony, anhydrite, fluorite, and strontianite tend to move closer to the equilibrium line (SI = 0) from approximately 105–180°C, at which temperatures these minerals are assumed to be in equilibrium with thermal waters, giving rise to the estimated reservoir temperature. Similarly, for the Shenzao thermal waters, the SIs with respect to anhydrite, quartz, strontianite, chalcedony, fluorite, and gypsum converge to the zero line at temperatures of 100–165°C. However, note that samples from Shenzao attain equilibration with calcite, aragonite, fluorite, and gypsum at temperatures higher than 250°C, and the other hydrothermal minerals do not tend to intersect the equilibrium line close to a common temperature. These findings confirm that thermal waters from Shenzao are not well equilibrated, probably due to mixing with a much higher proportion of seawater than Xinzhou.

As dissolved aluminum was not analyzed, the curves of saturation relative to aluminosilicate minerals could not be integrated. To eliminate the effect caused by lacking Al, an approach was used which is named FixAl and was developed by Pang and Reed [69], which entails the construction of a modified $Q/K$ graph. In this case, the total dissolved carbonate content is computed by charge balance, thus correcting for some loss of $CO_2$, and the Al concentration is fixed by assuming equilibrium of the fluid with albite at all temperatures [66]. The results (Figures 10(c) and 10(d)) in temperature estimates are progressively better constrained and closer to the maximum calculated chalcedony temperatures of approximately 160°C for Xinzhou and 140°C for Shenzao.

The combination of anhydrite and chalcedony saturation indices allows identification of the equilibrium temperature of thermal waters, using the retrograde and prograde solubilities of anhydrite and chalcedony, respectively. Figures 10(e) and 10(f) demonstrate that anhydrite and chalcedony are both close to equilibrium in the temperature range of 148–162°C for Xinzhou and range of 135–144°C for Shenzao. Overall, this method is more suitable for the study area within a narrower temperature range than the former geothermometers.

*4.5. Conceptual Model of the Geothermal System.* This study of the chemical and isotopic compositions of the Xinzhou and Shenzao thermal waters allows us to construct a schematic cross-sectional fault-hydrology conceptual model as illustrated in Figure 11 with the assumed flow paths of the different types of water entering the aquifer (geothermal fluid, fresh groundwater, and seawater). The flow system originates mainly from a mixture of infiltrating meteoric waters and seawater, and the hydrothermal fluids have a great depth of circulation along the NE-striking deep fault and fractured network, which are well connected to the deep heat source. The deep fault, acting as a perfect geothermal channel of high permeability, serves as a base frame for thermal cycling of fluid flow and heat transfer. Another important factor that favors deep circulation is the driving force due to buoyancy generated by the large decreases in density and viscosity, with increases in temperature and pressure. After being heated at depth, this heated fluid ascends to the Yanshanian biotite granite, is cooled down through conductive heat loss, and is diluted by cold fresh groundwater joining the thermal circulation system at the eastern margin of the geothermal aquifer. At the western seaward margin of the aquifer, a dispersion zone occurs, where seawater and fresh water come into contact at an interface. The downflowing seawater runs parallel to the upflowing fresh water along the interface before they are captured by the convective thermal flow at fault intersections.

## 5. Conclusions

We have conducted hydrogeochemical characterization and studied geothermometry applicability for thermal waters from the Xinzhou and Shenzao geothermal fields in the coastal regions of southern China's Guangdong province. The basement of the geothermal field consists of Early Yanshanian biotite granites and granite porphyry which are covered by Miocene volcanics and Holocene and Late Pleistocene fluviodeltaic sediments, which provides superior conditions for geothermal resources. The geothermal fields in the coastal areas are tens of kilometers landward either from or on the shoreline. Our results show the effect of seawater intrusion which modified the thermal chemistry of the thermal waters. The major findings are as follows.

The chemical and physical characteristics of the thermal waters are distinctively different from those of cold shallow groundwaters. Thermal waters comprise two relatively similar hydrochemical types, Na-Cl and Ca-Na-Cl types, confirming the occurrence of extensive subsurface seawater intrusion. With respect to seawater, thermal waters present significant enrichments in Ca, Si, Li, Sr, and B, which are caused by the interaction of the solution with rocks, mainly through dissolutions of silicate minerals. The considerable depletions in Mg and $SO_4$ are contributed by intensive chloritization of the metasomatic biotite and precipitation of sulphate minerals or reduction to sulfide, respectively. In particular, the deficiencies in $SO_4$ and Mg suggest the occurrence of reducing conditions and relatively high temperatures. The negative oxidation-reduction potential values observed in the thermal waters also indicate a reducing environment at deep depth.

Cl and ions are highly correlated with isotopic characteristics of the thermal waters, reflecting the clear mixing trend with seawater and extensive fluid-rock interactions. Thermal waters originate mainly from infiltrating meteoric waters and have a great circulation depth along the NE-striking deep fault and interconnected fractured network. Such a fault might facilitate the intrusion of seawater into the geothermal system, even in the inland areas.

All thermal waters of the study areas are undersaturated with respect to anhydrite and gypsum, indicating that dissolution of the sulfate salts is an ongoing process. The thermal waters are oversaturation or nearly equilibria with respect to aragonite, calcite, chalcedony, dolomite, and quartz, indicating that precipitation of carbonate and silica minerals evidently has occurred. All thermal waters are far from the full equilibrium line in Giggenbach's triangular diagram, reflecting the mixing of cold waters. Chemical geothermometry applications, together with fluid-mineral equilibria calculations, yield the most reliable estimates of the reservoir temperatures lying in the range of 148–162°C for Xinzhou and the range of 135–144°C for Shenzao thermal waters.

A schematic cross-sectional fault-hydrology conceptual model has been constructed based on the hydrogeological information. Due to the existence of naturally high heat conduction and thermal convection from the heat source, after being heated at deep depth, the geothermal fluids ascend to the Yanshanian biotite granite unit via faults and fractures which act as hydrothermal pathways.

## Conflicts of Interest

The authors declare that they have no conflicts of interest.

## Acknowledgments

This study was financially supported by the National Natural Science Foundation of China (NSFC) (Grant no. 41572241) and partially by the China Geological Survey Project (no. 1212011220014), Research and Investigation of Geothermal-Controlling Geological Structures in the Pearl River Delta and Neighboring Regions, from the Water Engineering and Environment Division. The authors acknowledge Guangdong Provincial Hydrogeology Brigade for helping with access to unpublished data and assistance with fieldwork.

## References

[1] M. O. Awaleh, F. B. Hoch, I. H. Kadieh et al., "The geothermal resources of the Republic of Djibouti - I: Hydrogeochemistry of the Obock coastal hot springs," *Journal of Geochemical Exploration*, vol. 152, pp. 54–66, 2015.

[2] E. Dotsika, I. Leontiadis, D. Poutoukis, R. Cioni, and B. Raco, "Fluid geochemistry of the Chios geothermal area, Chios Island, Greece," *Journal of Volcanology and Geothermal Research*, vol. 154, no. 3-4, pp. 237–250, 2006.

[3] E. Dotsika, D. Poutoukis, and B. Raco, "Fluid geochemistry of the Methana Peninsula and Loutraki geothermal area, Greece," *Journal of Geochemical Exploration*, vol. 104, no. 3, pp. 97–104, 2010.

[4] G. Tarcan and Ü. Gemici, "Water geochemistry of the Seferihisar geothermal area, İzmir, Turkey," *Journal of Volcanology and Geothermal Research*, vol. 126, no. 3-4, pp. 225–242, 2003.

[5] A. Vengosh, C. Helvaci, and I. H. Karamanderesi, "Geochemical constraints for the origin of thermal waters from western Turkey," *Applied Geochemistry*, vol. 17, no. 3, pp. 163–183, 2002.

[6] F. Magri, T. Akar, U. Gemici, and A. Pekdeger, "Numerical investigations of fault-induced seawater circulation in the Seferihisar-Balçova Geothermal system, western Turkey," *Hydrogeology Journal*, vol. 20, no. 1, pp. 103–118, 2012.

[7] T. Gurav, H. K. Singh, and D. Chandrasekharam, "Major and trace element concentrations in the geothermal springs along the west coast of Maharashtra, India," *Arabian Journal of Geosciences*, vol. 9, no. 1, article no. 44, pp. 1–15, 2016.

[8] F. Risacher, B. Fritz, and A. Hauser, "Origin of components in Chilean thermal waters," *Journal of South American Earth Sciences*, vol. 31, no. 1, pp. 153–170, 2011.

[9] R. Chandrajith, J. A. C. Barth, N. D. Subasinghe, D. Merten, and C. B. Dissanayake, "Geochemical and isotope characterization of geothermal spring waters in Sri Lanka: Evidence for steeper than expected geothermal gradients," *Journal of Hydrology*, vol. 476, pp. 360–369, 2013.

[10] A. Lashin, D. Chandrasekharam, N. Al Arifi, A. Al Bassam, and C. Varun, "Geothermal energy resources of wadi Al-Lith, Saudi Arabia," *Journal of African Earth Sciences*, vol. 97, pp. 357–367, 2014.

[11] J. F. Yuan, X. M. Mao, and Y. X. Wang, "Hydrogeochemical Characteristics of Low to Medium Temperature Groundwater in the Pearl River Delta Region, China," *Procedia Earth Planetary Science*, vol. 7, pp. 928–931, 2013.

[12] H.-Q. Huang, X.-H. Li, Z.-X. Li, and W.-X. Li, "Intraplate crustal remelting as the genesis of Jurassic high-K granites in the coastal region of the Guangdong Province, SE China," *Journal of Asian Earth Sciences*, vol. 74, pp. 280–302, 2013.

[13] O. A. Critchett, "Geothermal resources and the continuous operation of power station for the last decade in Fengshun county Guangdong Province," *Acta Energiae Solaris Sinica*, 1995.

[14] G. Zhang, C.-Q. Liu, H. Liu, Z. Jin, G. Han, and L. Li, "Geochemistry of the Rehai and Ruidian geothermal waters, Yunnan Province, China," *Geothermics*, vol. 37, no. 1, pp. 73–83, 2008.

[15] G. Lu and R. Liu, "Aqueous chemistry of typical geothermal springs with deep faults in Xinyi and Fengshun in Guangdong Province, China," *Journal of Earth Science*, vol. 26, no. 1, pp. 60–72, 2015.

[16] Bureau of Geology and Mineral Resources of Guangdong Province, *Regional geology of Guangdong province, People's Republic of China*, Geology Publishing House, Beijing, China, 1988.

[17] S. Pastorelli, L. Marini, and J. C. Hunziker, "Water chemistry and isotope composition of the Acquarossa thermal system, Ticino, Switzerland," *Geothermics*, vol. 28, no. 1, pp. 75–93, 1999.

[18] Z. Sun, A. Wang, J. Liu, B. Hu, and J. Chen, "Radiogenic Heat Production of Granites and Potential for Hot Dry Rock Geothermal Resource in Guangdong Province, Southern China," in *Proceedings of the Proceedings World Geothermal Congress*, Melbourne, Australia, 2015.

[19] X. M. Zhou and W. X. Li, "Origin of late mesozoic igneous rocks in Southeastern China: implications for lithosphere subduction and underplating of mafic magmas," *Tectonophysics*, vol. 326, no. 3-4, pp. 269–287, 2000.

[20] X. Zhou, T. Sun, W. Shen, L. Shu, and Y. Niu, "Petrogenesis of Mesozoic granitoids and volcanic rocks in South China: a response to tectonic evolution," *Episodes*, vol. 29, no. 1, pp. 26–33, 2006.

[21] L. Chen, T. Ma, Y. Du et al., "Hydrochemical and isotopic (2H, 18O and 37Cl) constraints on evolution of geothermal water in coastal plain of Southwestern Guangdong Province, China," *Journal of Volcanology and Geothermal Research*, vol. 318, pp. 45–54, 2016.

[22] J. Guo, X. Mao, S. Tong, and L. Feng, "Using hydrochemical geothermometers calculate exchange temperature of deep geothermal system in west coastal area of Guangdong Province," *Diqiu Kexue - Zhongguo Dizhi Daxue Xuebao/Earth Science - Journal of China University of Geosciences*, vol. 41, no. 12, pp. 2075–2087, 2016.

[23] R. O. Fournier, "Chemical geothermometers and mixing models for geothermal systems," *Geothermics*, vol. 5, no. 1-4, pp. 41–50, 1977.

[24] S. P. Verma and E. Santoyo, "New improved equations for Na/K, Na/Li and SiO2 geothermometers by outlier detection and rejection," *Journal of Volcanology and Geothermal Research*, vol. 79, no. 1-2, pp. 9–23, 1997.

[25] W. F. Giggenbach, "Geothermal solute equilibria. Derivation of Na-K-Mg-Ca geoindicators," *Geochimica et Cosmochimica Acta*, vol. 52, no. 12, pp. 2749–2765, 1988.

[26] R. O. Fournier and A. H. Truesdell, "An empirical NaKCa geothermometer for natural waters," *Geochimica et Cosmochimica Acta*, vol. 37, no. 5, pp. 1255–1275, 1973.

[27] C. Fouillac and G. Michard, "Sodium/lithium ratio in water applied to geothermometry of geothermal reservoirs," *Geothermics*, vol. 10, no. 1, pp. 55–70, 1981.

[28] H. Yaoli and M. Chu, "On the relations between the features of geological formation and the geomorohic growth in Guangdong Province," *Yunnan Geographic Environment Research*, vol. 75, no. 13, pp. 4398–4409, 1995.

[29] K.-Y. Kim, H. Seong, T. Kim et al., "Tidal effects on variations of fresh-saltwater interface and groundwater flow in a multilayered coastal aquifer on a volcanic island (Jeju Island, Korea)," *Journal of Hydrology*, vol. 330, no. 3-4, pp. 525–542, 2006.

[30] C. Appelo and D. Postma, *Geochemistry, groundwater and pollution*, 2nd edition, 2005.

[31] R. C. Arthur, T. Iwatsuki, E. Sasao, R. Metcalfe, K. Amano, and K. Ota, "Geochemical constraints on the origin and stability of the Tono Uranium Deposit, Japan," *Geochemistry: Exploration, Environment, Analysis*, vol. 6, no. 1, pp. 33–48, 2006.

[32] S. Arnórsson and I.A.E. Agency, *Isotopic and chemical techniques in geothermal exploration, development and use : sampling methods, data handling, interpretation*, International Atomic Energy Agency, 2000.

[33] D. B. N. Wishart, *Comparison of Silica and Cation Geothermometers of Bath Hot Springs, Jamaica WI*, World Geothermal Congress, 2015.

[34] A. J. Ellis and W. A. J. Mahon, *Chemistry and Geothermal Systems*, Academic Press, 1977.

[35] K. Pruess, C. M. Oldenburg, and G. Moridis, *TOUGH2 User's Guide*, 2011.

[36] A. Frumkin and H. Gvirtzman, "Cross-formational rising groundwater at an artesian karstic basin: The Ayalon Saline Anomaly, Israel," *Journal of Hydrology*, vol. 318, no. 1-4, pp. 316–333, 2006.

[37] U. Lauber and N. Goldscheider, "Use of artificial and natural tracers to assess groundwater transit-time distribution and flow systems in a high-alpine karst system (Wetterstein Mountains, Germany)," *Hydrogeology Journal*, vol. 22, no. 8, pp. 1807–1824, 2014.

[38] J. Wang, M. Jin, B. Jia, and F. Kang, "Hydrochemical characteristics and geothermometry applications of thermal groundwater in northern Jinan, Shandong, China," *Geothermics*, vol. 57, pp. 185–195, 2015.

[39] G. Michard, "Behaviour of major elements and some trace elements (Li, Rb, Cs, Sr, Fe, Mn, W, F) in deep hot waters from granitic areas," *Chemical Geology*, vol. 89, no. 1-2, pp. 117–134, 1990.

[40] H. Alçiçek, A. Bülbül, and M. C. Alçiçek, "Hydrogeochemistry of the thermal waters from the Yenice Geothermal Field (Denizli Basin, Southwestern Anatolia, Turkey)," *Journal of Volcanology and Geothermal Research*, vol. 309, pp. 118–138, 2016.

[41] A. A. El-Fiky, "Hydrogeochemistry andGeothermometry of thermal groundwater from the Gulf of Suez region, Egypt," *Journal of King Abdulaziz University, Earth Sciences*, vol. 20, no. 2, pp. 71–96, 2009.

[42] K. Nicholson, *Geothermal fluids: chemistry and exploration techniques*, Springer Berlin Heidelberg, Berlin, Heidelberg, 1993.

[43] Q. Guo and Y. Wang, "Geochemistry of hot springs in the Tengchong hydrothermal areas, Southwestern China," *Journal of Volcanology and Geothermal Research*, vol. 215-216, pp. 61–73, 2012.

[44] R. L. Linnen, C. Galeschuk, and N. M. Halden, *The use of fracture minerals to define metasomatic aureoles around rare-metal pegmatites. Fracture Chlorites in Exploration*, IAGS, 27th edition.

[45] S.-G. Lee, T.-K. Kim, J.-S. Lee, T. J. Lee, B. W. Cho, and H. J. Koh, "Geochemical implication of 87Sr/86Sr ratio of high-temperature deep groundwater in a fractured granite aquifer," *Geochemical Journal*, vol. 42, no. 5, pp. 429–441, 2008.

[46] P. Kumar, C. K. Singh, C. Saraswat, B. Mishra, and T. Sharma, *Evaluation of aqueous geochemistry of fluoride enriched groundwater: A case study of the Patan district, Gujarat, Western India*, Water Science, 2017.

[47] A. Minissale, G. Magro, O. Vaselli, C. Verrucchi, and I. Perticone, "Geochemistry of water and gas discharges from the Mt. Amiata silicic complex and surrounding areas (central Italy)," *Journal of Volcanology and Geothermal Research*, vol. 79, no. 3-4, pp. 223–251, 1997.

[48] W. M. Edmunds, "Bromine geochemistry of British groundwaters," *Mineralogical Magazine*, vol. 60, no. 2, pp. 275–284, 1996.

[49] R. E. Diamond and C. Harris, "Oxygen and hydrogen isotope geochemistry of thermal springs of the Western Cape, South Africa: Recharge at high altitude?" *Journal of African Earth Sciences*, vol. 31, no. 3-4, pp. 467–481, 2000.

[50] H. Craig, "Isotopic variations in meteoric waters," *Science*, vol. 133, no. 3465, pp. 1702-1703, 1961.

[51] A. H. Truesdell and J. R. Hulston, "Chapter 5-isotopic evidence on environments of geothermal systems," *Terrestrial Environment A*, pp. 179–226, 1980.

[52] R. J. Motyka, C. J. Nye, D. L. Turner, and S. A. Liss, "The geyser bight geothermal area, Umnak Island, Alaska," *Geothermics*, vol. 22, no. 4, pp. 301–327, 1993.

[53] G. Lu, E. L. Sonnenthal, and G. S. Bodvarsson, "Multiple component end-member mixing model of dilution: Hydrochemical effects of construction water at Yucca Mountain, Nevada, USA," *Hydrogeology Journal*, vol. 16, no. 8, pp. 1517–1526, 2008.

[54] D. L. Parkhurst and C. A. J. Appelo, "User's guide to PHREEQC - a computer program for speciation,batch-reaction, one-dimensional transport, and inversegeochemical calculations," *U.s.geological Survey Water Resources Investigations Report*, vol. 99, 1999.

[55] D. K. Nordstrom and E. A. Jenne, "Fluorite solubility equilibria in selected geothermal waters," *Geochimica et Cosmochimica Acta*, vol. 41, no. 2, pp. 175–188, 1977.

[56] W. Jang, "TOUGHREACT-A simulation program for non-isothermal multiphase reactive geochemical transport in variably saturated geologic media: Applications to geothermal injectivity and CO2 geological sequestration," *Computers & Geosciences*, vol. 32, no. 2, pp. 145–165, 2006.

[57] R. O. Fournier, "A revised equation for Na/K geothermometer," in *Proceedings of the Expanding the Geothermal Frontier, Transactions Volume 3, Geothermal Resources Council Annual Meeting.*, pp. 221–224.

[58] R. O. Fournier and R. W. Potter II, "Magnesium correction to the NaKCa chemical geothermometer," *Geochimica et Cosmochimica Acta*, vol. 43, no. 9, pp. 1543–1550, 1979.

[59] K. Pandarinath, "Solute geothermometry of springs and wells of the Los Azufres and Las Tres Virgenes geothermal fields, Mexico," *International Geology Review*, vol. 53, no. 9, pp. 1032–1058, 2011.

[60] A. Y. García-Soto, K. Pandarinath, J. E. Marrero-Ochoa, and C. Díaz-Gómez, "Solute geothermometry of Cerro Prieto and Los Humeros geothermal fields, Mexico: considerations on chemical characteristics of thermal water," *Arabian Journal of Geosciences*, vol. 9, no. 8, article no. 517, 2016.

[61] R. W. Henley, "Fluid Mineral Equilibria in Hydrothermal Systems," *Reviews in Economic Geology*, vol. 1, 1984.

[62] F. Xu and L. Guo, "The Aqueous Chemistry and Hydrodynamic Characteristics of Brackish Waters in the Xinzhou Geothermal Field, Coastal Guangdong," *Safety and Environmental Engineering*, vol. 24, no. 1, pp. 1–10, 2017.

[63] J. F. Yuan, *Hrodrogeochemistry of the Geothermal system in Coastal Areas of Guangdong Province, South China*, China University of Geoscicences, 2013.

[64] M. H. Reed, "Calculation of multicomponent chemical equilibria and reaction processes in systems involving minerals, gases and an aqueous phase," *Geochimica et Cosmochimica Acta*, vol. 46, no. 4, pp. 513–528, 1982.

[65] N. Spycher, L. Peiffer, E. L. Sonnenthal, G. Saldi, M. H. Reed, and B. M. Kennedy, "Integrated multicomponent solute geothermometry," *Geothermics*, vol. 51, pp. 113–123, 2014.

[66] L. Peiffer, C. Wanner, N. Spycher, E. L. Sonnenthal, B. M. Kennedy, and J. Iovenitti, "Optimized multicomponent vs. classical geothermometry: Insights from modeling studies at the Dixie Valley geothermal area," *Geothermics*, vol. 51, pp. 154–169, 2014.

[67] G. Neupane, J. S. Baum, E. D. Mattson, G. L. Mines, C. D. Palmer, and R. W. Smith, "Validation of Multicomponent Equilibrium Geothermometry at Four Geothermal Power Plants," *Fortieth Workshop on Geothermal Reservoir Engineering, Stanford University*, 2001.

[68] C. D. Palmer, S. R. Ohly, R. W. Smith, G. Neupane, T. McLing, and E. Mattson, "Mineral selection for multicomponent equilibrium geothermometry," in *Proceedings of the Geothermal Resources Council Annual Meeting - Geothermal: A Global Solution, GRC 2014*, pp. 453–459, usa, October 2014.

[69] Z.-H. Pang and M. Reed, "Theoretical chemical thermometry on geothermal waters: problems and methods," *Geochimica et Cosmochimica Acta*, vol. 62, no. 6, pp. 1083–1091, 1998.